Computer Methods in Applied Mechanics and Engineering 450 (2026) 118676

Contents lists available at ScienceDirect

Computer Methods in Applied Mechanics and Engineering

journal homepage: www.elsevier.com/locate/cma

Resolved CFD-DEM for high-fidelity multiphase flow modeling in porous media of arbitrary geometry

Tao Yu *, Jidong Zhao *

The Hong Kong University of Science and Technology, Clearwater Bay, Kowloon, Hong Kong

ARTICLE INFO

Keywords:
Coupled CFD-DEM
Porous media modeling
Multiphase flow dynamics
Wave-structure interaction
Coastal engineering

ABSTRACT

The design of resilient coastal infrastructure requires high-fidelity modelling of complex interactions between waves, porous structures, and mobile seabed. To address this need, we develop a novel computational framework that couples Computational Fluid Dynamics (CFD) and the Discrete Element Method (DEM), explicitly integrating a resolved porous media module. This approach enables direct numerical simulation of multiphase flows and their particle-scale interactions with both stationary and mobile porous structures, such as breakwaters or armor units. The model is rigorously validated against six benchmark cases, demonstrating robust capabilities in capturing permeability, capillary effects, and fluid–solid momentum exchange. We further apply the framework to large-scale coastal scenario featuring realistic wave generation, curved and trapezoidal seawalls, and over one hundred mobile cubic armor units. The simulations provide deep insights into critical processes like wave reflection, entrapped air dynamics, and drag-induced energy dissipation. The simulation results quantitatively show that porous structures significantly enhance wave energy dissipation, leading to superior wave attenuation. This integrated framework represents a significant advancement for high-fidelity, efficient simulations of fluid–structure interactions in dynamic and porous coastal environments, with great potential for coastal engineering design and environmental fluid mechanics.

1. Introduction

Porous structures serve as fundamental dynamic interfaces for energy dissipation and load redistribution in coastal protection systems and geotechnical infrastructure. In marine environments, these structures include floating breakwaters [1,2], seawall-embankment integrated systems [3,4], rubble-mound barriers [5,6], and perforated seawalls [7], all leveraging interstitial fluid–structure interactions to attenuate wave energy and mitigate erosion. Analogous geotechnical systems, such as granular filters in earth dams [8] and ballast layers [9], similarly rely on pore-scale mechanics to regulate seepage forces and ensure stability. These innovations underscore the critical role of multiphase flow dynamics in optimizing porous structure performance across scales. For instance, floating breakwaters exemplify adaptive porous marine structures where wave attenuation arises from both dynamic buoyancy responses and material porosity [10]. Similarly, modern seawall-embankment hybrid systems incorporate permeable cores within traditional coastal defenses to concurrently dissipate wave energy and prevent hinterland flooding [11].

These dual imperatives have motivated decades of research, as comprehensively reviewed in seminal works on analytical and numerical approaches [12,13]. Engineering analyses have long relied on macroscopic porous media flow behavior, where force

* Corresponding authors.
E-mail addresses: tyuak@connect.ust.hk (T. Yu), jzhao@ust.hk (J. Zhao).

https://doi.org/10.1016/j.cma.2025.118676
Received 2 September 2025; Received in revised form 29 November 2025; Accepted 13 December 2025

formulations derived from experimental observations govern numerical implementations. Pioneering studies by Darcy [14], Forchheimer [15], and Polubarinova-Kochina [16] established seminal foundational models, including linear drag, quadratic inertial resistance, and transient acceleration terms, that have been widely used to quantify fluid-porous interactions through empirical coefficients. These formulations were systematically integrated into computational frameworks as momentum source terms, homogenizing porous zones into "sponge" regions in CFD models. This paradigm has advanced simulations of fixed porous structures like rubble-mound breakwaters in coastal engineering [17,18]. However, treating porous media as static proves inadequate for floating structures, where dynamic fluid–structure interactions necessitate resolution of intra-wave force fluctuations and six-degree-of-freedom (6DoF) motions.

The emergence of innovative coastal defenses (e.g., porous floating breakwaters, hybrid armor-seawall systems) has exposed critical gaps in numerical capabilities. While experimental advancements, such as perforated membranes and diamond-shaped units, demonstrate enhanced wave dissipation [19,20], existing numerical frameworks face three fundamental challenges: (1) reformulating force closure models to account for relative fluid–structure velocities; (2) resolving nonlinear interactions between air–water interfaces and porous units during wave breaking; and (3) addressing discontinuous permeability fields in systems combining permeable and impermeable elements (e.g., armor units adjacent to solid seawalls).

Multiscale numerical modeling of porous media generally falls into two categories: discrete models, which explicitly resolve internal pore-scale geometries, and continuum models, which homogenize the porous structure via averaging techniques [21–23]. While discrete approaches enable high-fidelity pore-scale analysis and continuum methods are efficient for large-scale scenarios, both conventionally assume a stationary porous domain. This inherent limitation preclude the simulation of dynamic structural displacement [24]. Consequently, classical CFD techniques, including volume-of-fluid (VOF)-based finite-volume solvers [25,26], smoothed particle hydrodynamics (SPH) [27,28], and the lattice Boltzmann method (LBM) [29,30], are typically confined to modeling fluid infiltration within static matrices. More recently, machine-learning frameworks have emerged to rapidly predict porous media-fluid interactions, such as dynamic wave propagation [31,32], by learning reduced-order representations from high-fidelity simulations. However, these data-driven models also largely rely on the assumption of static porous domains. Thus, a fundamental challenge persists: the accurate representation of fully dynamic porous structures, where fluid flow and solid displacement are intrinsically coupled, remains beyond the scope of most existing numerical and data-driven approaches.

Modeling fully dynamic systems represents a persistent challenge in computational mechanics, with established methodologies facing significant limitations. For instance, Dong et al. [33] developed a coupled CFD-RBD (rigid-body dynamics) framework to simulate wave interactions with porous floating breakwaters. While being a step forward, their formulation is not readily generalizable to systems with mixed permeable/impermeable boundaries or arbitrary geometric complexity. The CFD-DEM (discrete element method) coupling offers greater adaptability by resolving the motion of and interactions among numerous discrete bodies alongside the fluid-particle dynamics [34]. However, a fundamental constraint of prevailing CFD-DEM schemes is their treatment of impermeable particle assemblies as a impermeably, discrete medium [35–38]. Critically, unlike the CFD-RBD paradigm wherein rigid bodies can be assigned intrinsic porous properties, standard CFD-DEM cannot represent individual particles or structures as porous entities. Furthermore, the computational cost of achieving high-fidelity resolution of interparticle or interstructural fluid flow in such systems is often prohibitive [39]. These issues collectively form a major conceptual and technical barrier to the large-scale simulation of fully dynamic, multiscale porous systems with authentic structural mobility.

To overcome these limitations, especially, the inability to handle mixed mobile and stationary permeable/impermeable bodies with arbitrary geometries, and their prohibitive computational cost for large-scale applications, this study introduces a unified, GPU-accelerated CFD-DEM framework for fully dynamic porous systems. Our approach fundamentally departs from conventional formulations by explicitly resolving mobile and stationary porous structures, impermeable bodies, and their interactions within multiphase flows. Key innovation of the framework include: (1) The treatment of individual structural units as either porous or impermeable media; (2) Particle-scale hydrodynamic force computation and two-way fluid-structure coupling; (3) Adaptive porosity mapping for hybrid configurations (e.g., layered rubble mounds adjacent to rigid seawalls). (4) An embedded six-degree-of-freedom (6DoF) solver for high-fidelity transient wave-induced motions and structural dynamics. The framework is rigorously verified through six benchmark cases spanning three critical regimes: stationary porous media, stationary porous-fluid interactions, and dynamic porous structure–-fluid interactions. These validations systematically verify the model's capabilities in resolving porous media hydrodynamics (including permeability and capillary forces), multiphase flow transitions, and CFD-DEM integration. Building on this foundation, we demonstrate engineering applicability via a large-scale coastal defense simulation incorporating wave generation, air-water phase dynamics, curved/trapezoidal seawalls, and over 100 mobile cubic armor units. This case study confirms the methodology's robustness in handling real-world complexities involving coexisting stationary/mobile porous structures and multiphase flows.

The paper is structured as follows: Section 2 introduces the resolved CFD-DEM framework incorporating porous media, including a comparison with the multiphase porous media model and the integration of CFD and DEM components. Section 3 verifies the framework using benchmark cases involving multiphase flows and stationary/moving porous structures, with quantitative accuracy assessment. Section 4 applies the framework to a complex wave-armor unit-seawall system, demonstrating real-world coastal engineering applicability.

2. Methodology: resolved CFD-DEM framework for porous media

2.1. Multiphase model with porous media

In this study, porous structures are modeled as a homogenized continuum material with spatially uniform porosity and

permeability [21]. Following established classifications [22,23], we categorize the media into two types based on pore-scale geometry and dominant flow regime: (1) Type A: This category includes coarse-grained, open structures with relatively large pores or flow passages, such as porous breakwaters, rubble-mound structures, and wave-dissipating blocks, where flow through large pores occurs at higher velocities and inertial effects are significant. (2) Type B: This category encompasses fine-grained materials such as soils and loosely packed granular sands or gravels, where flow is characterized by low-velocity infiltration and capillary forces. For flow in Type A porous media, the Darcy-Forchheimer equation [33] captures nonlinear inertial effects, with capillary forces deemed negligible and thus excluded from the model. Conversely, Type B porous media necessitate advanced modeling to address critical capillary effects. Here, the Brooks-Corey and van Genuchten models [40] characterize both the permeability-dominated and capillary-dominated flow under unsaturated conditions. In this study, multiphase modeling approaches are tailored to each type, with conventional algorithms modified for Type B to incorporate capillarity.

The simulation of multiphase flow employs the Volume of Fluid (VOF) method in conjunction with the MULES algorithm [41,42], which tracks phase distribution through volume fractions (α_i) and integrates a compressive flux term into the advection equation to enhance interface resolution. The continuity equation governing volume fraction transport in porous media [40] incorporates this compressive term (Eq. (1)). Assuming incompressible fluids, the continuity equation is expressed as:

$$\frac{\partial \phi \alpha_i}{\partial t} + \nabla \cdot \left(\alpha_i \mathbf{u}_\mathrm{f}\right) + \nabla \cdot \left(\phi \alpha_i (1-\alpha_i)\mathbf{u}_\mathrm{c}\right) = 0, \tag{1}$$

where ϕ is porosity of porous media and t is the time. $\mathbf{u}_\mathrm{f}$ is the fluid velocity and $\mathbf{u}_\mathrm{c}$ is the compressed velocity.

The computation of the compressive flux term is location-dependent: in pure fluid regions and Type A porous media, it is determined using the conventional MULES algorithm, whereas for Type B porous media, the approach proposed by Francisco et al. [40] is adopted due to the dominant role of capillary forces.

$$\mathbf{u}_\mathrm{c} = \begin{cases} c|\mathbf{u}_\mathrm{f}|\nabla\alpha_i/|\nabla\alpha_i|, & \textit{in pure fluid regions and Type A porous media}, \\ \phi^{-1}\begin{bmatrix} -\left(\dfrac{M_i}{\alpha_i} - \dfrac{M_j}{\alpha_j}\right)\nabla p + \left(\dfrac{\rho_i M_i}{\alpha_i} - \dfrac{\rho_j M_j}{\alpha_j}\right) g + \\ \left(\dfrac{M_i \alpha_j}{\alpha_i} + \dfrac{M_j \alpha_i}{\alpha_j}\right)\nabla p_\mathrm{c} - \left(\dfrac{M_i}{\alpha_i} - \dfrac{M_j}{\alpha_j}\right) p_\mathrm{c} \nabla \alpha_i \end{bmatrix}, & \textit{in Type B porous media}, \end{cases} \tag{2}$$

where $c \in [0,\ 1]$ is the coefficient to control the compressed velocity. The subscripts i and j denote fluid phase i and fluid phase j, respectively. $\mathbf{g}$, M and ρ denotes the gravity, mobility and density, respectively. p is the fluid pressure and p_c is the capillary pressure.

The capillary pressure p_c and mobility M are determined based on the capillary pressure and relative permeability models, respectively. In this study, we adopt the models proposed by van Genuchten [43] and Brooks and Corey [44], as defined in Eqs. (3) to (8).

$$p_\mathrm{c} = p_{\mathrm{c},0}\alpha_{i,\mathrm{pc}}^{-\beta}\ (\mathrm{Brooks-Corey\ model}), \tag{3}$$

$$p_\mathrm{c} = p_{\mathrm{c},0}\left(\alpha_{i,\mathrm{pc}}^{-1/m} - 1\right)^{1-m}\ (\mathrm{van\ Genuchten\ model}), \tag{4}$$

$$\alpha_{i,\mathrm{pc}} = \frac{\alpha_i - \alpha_{\mathrm{pc,irr}}}{\alpha_{\mathrm{pc,max}} - \alpha_{\mathrm{pc,irr}}} \tag{5}$$

where $p_{\mathrm{c},0}$ is the entry capillary pressure. β and m are the model parameters. $\alpha_{\mathrm{pc,max}}$ and $\alpha_{\mathrm{pc,irr}}$ denote the maximum saturation and the irreducible saturation of the fluid phase i, respectively.

$$\begin{cases} M_i = \dfrac{k_0}{\mu_i}k_{ri} = \dfrac{k_0}{\mu_i}\left(\alpha_{i,\mathrm{eff}}\right)^m \\ M_j = \dfrac{k_0}{\mu_j}k_{rj} = \dfrac{k_0}{\mu_j}\left(1-\alpha_{i,\mathrm{eff}}\right)^m \end{cases} (\mathrm{Brooks-Corey\ model}), \tag{6}$$

$$\begin{cases} M_i = \dfrac{k_0}{\mu_i}k_{ri} = \dfrac{k_0}{\mu_i}\alpha_{i,\mathrm{eff}}^{\frac{1}{2}}\left(1-\left(1-\alpha_{i,\mathrm{eff}}^{\frac{1}{m}}\right)^m\right)^2 \\ M_j = \dfrac{k_0}{\mu_j}k_{rj} = \dfrac{k_0}{\mu_j}\left(1-\alpha_{i,\mathrm{eff}}\right)^{\frac{1}{2}}\left(1-\alpha_{i,\mathrm{eff}}^{\frac{1}{m}}\right)^{2m} \end{cases} (\mathrm{van\ Genuchten\ model}), \tag{7}$$

$$\alpha_{i,\mathrm{eff}} = \frac{\alpha_i - \alpha_{i,\mathrm{irr}}}{1 - \alpha_{j,\mathrm{irr}} - \alpha_{i,\mathrm{irr}}} \tag{8}$$

where k_0 is the absolute permeability of the porous media. m is the model parameter. μ is the fluid viscosity. $\alpha_{i,\mathrm{irr}}$ denotes the irreducible saturation of the fluid phase i.

The equivalent density ρ and viscosity μ across the entire CFD domain are updated using the VOF algorithm and the permeability model.

$$\rho = \begin{cases} \alpha_1\rho_1 + \alpha_2\rho_2, \text{ in pure fluid regions and Type A porous media,} \\ (M_1 + M_2)^{-1}(M_1\rho_1 + M_2\rho_2), \text{ in Type B porous media,} \end{cases} \tag{9}$$

$$\mu = \alpha_1\mu_1 + \alpha_2\mu_2 \tag{10}$$

2.2. Momentum equations of coupled CFD-DEM

Unlike the conventional Navier–Stokes equations, when considering resolved CFD-DEM and porous media, the porosity ϕ and drag force $\mathbf{f}_d$ must be incorporated into the following momentum equation.

$$\phi^{-1}\left(\frac{\partial}{\partial t}(\rho\mathbf{u}_f) + \nabla\cdot\left(\phi^{-1}\rho\mathbf{u}_f\otimes\mathbf{u}_f\right)\right) = -\nabla p + \nabla\cdot\left(\phi^{-1}\mu\cdot\left(\nabla\mathbf{u}_f\right)\right) + \mathbf{f}_c + \mathbf{f}_d, \tag{11}$$

where ρ, $\mathbf{u}_f$ and p represent the density, velocity, and pressure of fluid, respectively. p is defined as $p = p_d + \rho g h$, where p_d is the dynamic pressure, g is the gravitational acceleration, and h is the reference height [45]. $\mathbf{f}_c$ and $\mathbf{f}_d$ represent the surface tension and the drag force in the porous media, respectively.

The surface tension $\mathbf{f}_c$ is computed by the following equation. In pure fluid regions, this term is computed using the conventional surface tension formulation, whereas in porous media, it is determined based on the capillary model.

$$\mathbf{f}_c = \begin{cases} \phi^{-1}c\sigma|\nabla\alpha_1|n, \text{ in pure fluid regions and Type A porous media,} \\ \left[(M_1 + M_2)^{-1}(M_1\alpha_2 - M_2\alpha_1)\dfrac{\partial p_c}{\partial\alpha_1} - p_c\right]\nabla\alpha_1, \text{ in Type B porous media,} \end{cases} \tag{12}$$

where σ denotes the surface tension coefficient, and c represents the curvature of the fluid-gas interface, defined as $c = -\nabla\cdot\mathbf{n}$, with $\mathbf{n}$ being the unit normal vector at the interface. For a free surface, $\mathbf{n}$ is computed as $\mathbf{n} = \nabla\alpha_1/|\nabla\alpha_1|$, while on a boundary face, $\mathbf{n}$ is set to $\mathbf{n} = \mathbf{n}_c$, reconstructed according to the specified contact angle. The capillary pressure p_c is determined using Eqs. (3) and (4).

Accurate computation of the contact angle at solid boundaries is critical in two-phase flow simulations, as it directly affects the fidelity of interface tracking and associated physical phenomena. Within the VOF-based framework, the prescribed contact angle is imposed by reconstructing the interface normal vector $\mathbf{n}_c$ at boundary faces. This corrected interface normal $\mathbf{n}_c$ is formulated as a linear combination:

$$\mathbf{n}_c = a\mathbf{n}_{wall} + b\mathbf{n}, \tag{13}$$

where $\mathbf{n}_{wall}$ denotes the unit normal vector of the solid boundary. The coefficients a and b are determined by satisfying two constraints: orthogonality and angular continuity. Specifically, the reconstructed interface normal vector $\mathbf{n}_c$ must satisfy $\mathbf{n}_c\cdot\mathbf{n}_{wall} = \cos\theta_{eq}$ and $\mathbf{n}_c\cdot\mathbf{n} = \cos\Delta\theta$, where $\Delta\theta = \theta_{now} - \theta_{eq}$. Here, θ_{eq} is the target contact angle, and θ_{now} is the current contact angle, defined as $\theta_{now} = \arccos(\mathbf{n}\cdot\mathbf{n}_{wall})$. By solving this system, the coefficients a and b can be obtained as follows:

$$a = \frac{\cos\theta - \cos\theta_{now}\cdot\cos\Delta\theta}{1 - (\cos\theta_{now})^2}, \tag{14}$$

$$b = \frac{\cos\Delta\theta - \cos\theta_{now}\cdot\cos\theta}{1 - (\cos\theta_{now})^2}, \tag{15}$$

The drag force $\mathbf{f}_d$ consists of two components: one induced by permeability ($\mathbf{f}_{d1}$) and the other by turbulence ($\mathbf{f}_{d2}$). The permeability-induced drag force $\mathbf{f}_{d1}$ can be further classified based on the porosity, as shown in Eq. (16). When the porosity is less than 0.01, representing a fully impermeable solid, the conventional resolved CFD-DEM drag force model is applied [34]. Conversely, when the porosity exceeds 0.01, indicating a porous medium, the drag force is determined using the permeability model [40]. The drag force $\mathbf{f}_{d2}$ can be written as $\mathbf{f}_{d2} = C_{d2}|\mathbf{u}_f|\mathbf{u}_f$ [46,47]. Since this quadratic drag term primarily accounts for inertial resistance in high Reynolds number flows, accurately determining the coefficient C_{d2} is often challenging due to its dependence on complex flow conditions. However, in Type B porous media, the flow is typically in the low Reynolds number regime, where viscous forces dominate and inertial effects are minimal. As a result, this term is neglected specifically for Type B cases, while retained for Type A where higher flow velocities and inertial contributions are more relevant.

$$\mathbf{f}_{d1} = \begin{cases} \left(\left(1 - \varepsilon_p^{\cdot}\right)\mathbf{u}_f^{\,n} + \varepsilon_p^{\cdot}\mathbf{v}^n - \mathbf{u}_f^{\,n+1}\right)\mathbf{A}_\mathbf{u}, \ (\phi < 0.01) \\ K_c\left(\left(1 - \varepsilon_p^{\cdot}\right)\mathbf{u}_f^{\,n} + \varepsilon_p^{\cdot}\mathbf{v}^n - \mathbf{u}_f^{\,n+1}\right), \ (\phi \geq 0.01) \end{cases}, \tag{16}$$

where $\varepsilon_p^{\cdot} = \frac{\rho_s}{\rho}\varepsilon_p$ is the density-equivalent fraction. $\mathbf{A}_\mathbf{u}$ represents the diagonal elements of the coefficient matrix formed after the discretization of Eq. (11). ε_p represents the solid fraction, which quantifies the volume fraction occupied by particles within a given

CFD cell. A solid fraction of 0 indicates that the cell is entirely outside a DEM particle, while a value of 1 signifies that the cell is completely contained within a DEM particle. ρ_s and ρ denote the densities of the solid particle and fluid, respectively. $\mathbf{v} = \mathbf{v}_p + \omega_p \times \mathbf{r}$, where $\mathbf{v}_p$ and ω_p represent the linear and angular velocities of Particle p, respectively. The vector $\mathbf{r}$ denotes the position vector extending from the particle's centroid to the center of the mesh cell. The coefficient K_c is defined as follows:

$$K_c = \begin{cases} C_{d1}\dfrac{(1-\phi)^2}{\phi^3}, & \text{in Type A porous media,} \\ k_0^{-1}\left(\dfrac{k_{ri}}{\mu_i}+\dfrac{k_{rj}}{\mu_j}\right)^{-1}, & \text{in Type B porous media,} \end{cases} \tag{17}$$

where C_{d1} is the permeability coefficient.

The motion of porous media is modeled using the Discrete Element Method (DEM) by solving the linear and angular momentum equations governing the motion of individual particles (Eq. (18)). Multiple interaction forces [48,49], including the particle–particle collision force $\mathbf{F}_{p-p}$, the particle-wall collision force $\mathbf{F}_{p-w}$, and the fluid–particle interaction force $\mathbf{F}_f$ [34], are considered in the model. The term $\omega_p \times (\mathbf{I}_p\omega_p)$ represents the gyroscopic torque that arises from the interaction between the inertia tensor distribution and the angular velocity, and it is specifically relevant for non-spherical particles. Unlike traditional resolved CFD-DEM methods, the fluid–particle interaction in this study also incorporates the porosity of the porous media ϕ, reflecting its impact on the flow dynamics and particle behavior.

$$\begin{cases} m_p\dfrac{d\mathbf{v}_p}{dt} = \mathbf{F}_f + m_p g + \sum \mathbf{F}_{p-p} + \sum \mathbf{F}_{p-w} \\ \mathbf{I}_p\dfrac{d\omega_p}{dt} + \omega_p \times (\mathbf{I}_p\omega_p) = \sum \mathbf{M}_t + \sum \mathbf{M}_r \\ \mathbf{F}_f = \sum_{j\in T_h}(1-\phi)\left(\dfrac{\rho_s}{\rho}\varepsilon_p(-\nabla p + \mu\rho\nabla^2 u_f) + \left(1-\dfrac{\rho_s}{\rho}\varepsilon_p\right)f_d\right)_j \cdot V_j \end{cases} \tag{18}$$

where m_p and $\mathbf{I}_p$ denote the mass and rotational inertia of Particle p, respectively. $\mathbf{M}_t$ and $\mathbf{M}_r$ correspond to the torque induced by the tangential force and the rolling friction torque [50], respectively.

The CFD-DEM coupling adopts separate time steps for the fluid and particle solvers. The CFD time step, Δt_{CFD}, is dynamically determined by the Courant-Friedrichs-Lewy (CFL) condition [51], maintaining a Courant number below 0.5 for numerical stability. In contrast, the DEM solver employs an explicit integration scheme and requires a significantly smaller time step, Δt_{DEM}. To reconcile the stability requirements with computational efficiency for both solvers, we implement sub-cycling for DEM. Following common practice in resolved CFD-DEM simulations [52], we set $\Delta t_{DEM} = \Delta t_{CFD}/10$. Thus, for each CFD step, the DEM solver performs ten sub-cycles to advance particle motion and contact forces before two phases synchronize to exchange momentum and volume-fraction data.

2.3. DEM for porous media of arbitrary geometry

Existing studies often treat porous media as a stationary solid [40] or consider only a single movable solid described by rigid body dynamics [33]. These simplifications greatly restrict the applicability of such methods in more complex engineering fields, such as coastal engineering. However, the proposed DEM algorithm with non-spherical particles enables the modeling of porous media with arbitrary shapes, allowing for high-accuracy and efficient simulation of the motion and collisions of porous solids interacting with fluids. Solving DEM with irregular-shaped particles requires addressing three key challenges: (1) the representation of irregular-shaped particles, (2) the collision model for irregular-shaped particles, and (3) the construction of the solid fraction field for irregular-shaped particles within CFD cells.

2.3.1. Representation of irregular geometry

Currently, in coupled CFD-DEM simulations, irregular-shaped particles are primarily represented using two approaches: (1) clumps composed of multiple spheres [53,54] and (2) spherical harmonics [55], and (3) polygonal or polyhedron based technique [56,57]. The clump-particle approach suffers from low computational efficiency and unrealistic contact parameters [58,59]. Spherical harmonics also have limited generality in representing diverse particle shapes. In this study, we adopt the STL format, which is one of the most versatile storage formats for arbitrary-shaped structures. The STL format represents structural information through a collection of triangular facets, making it well-suited for capturing complex geometries. Specifically, an STL file provides the coordinates of the three vertices (P_{i1} to P_{i3}) of each triangular facet within the structure, along with the normal vector ($\mathbf{n}_{fi}$) pointing outward from the exterior of the structure (Fig. 1).

2.3.2. Collision model

The collision modeling of irregular-shaped particles remains a significant research focus. The most common approach involves discretizing the particle surface into a series of points and applying conventional collision models, such as the Hertzian contact model. However, in this point-based discretization method, achieving high collision accuracy requires a high point density, leading to substantial computational costs. Additionally, since these collision models compute contact forces based on particle overlapping, they can

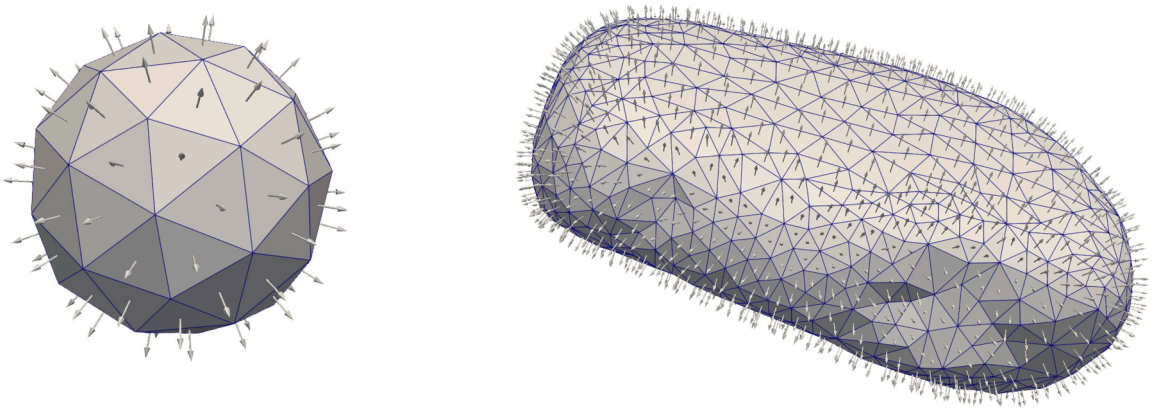

Fig. 1. Schematic of the structure described by the STL format, including triangular facets and the corresponding normal vectors pointing outward from each facet (as indicated by the arrows).

result in particle penetration, compromising physical accuracy.

In this study, we adopt a collision model based on the barrier-based method, which is derived from the Incremental Potential Contact (IPC) model [60]. This collision model has been widely employed in the finite element method [61] due to its four key advantages: (i) it does not introduce additional degrees of freedom or iterative steps, (ii) it ensures non-penetration, (iii) it avoids ill-conditioned matrix systems, and (iv) it allows direct control over solution accuracy. We extend this model to the contact modeling of irregular-shaped particles in DEM, enabling direct utilization of STL-format triangular mesh data for collision force computation. This approach eliminates the need for additional preprocessing of particle geometry, enhancing computational efficiency and accuracy. The normal contact force $\mathbf{F}_\mathrm{n}$ and the frictional force $\mathbf{F}_\mathrm{t}$ can be written as:

$$\mathbf{F}_\mathrm{n} = \begin{cases} k(d_\mathrm{n} - \widehat{d})\left[2\ln\left(\dfrac{d_\mathrm{n}}{\widehat{d}}\right) - \dfrac{\widehat{d}}{u_\mathrm{n}} + 1\right]\mathbf{n}_\mathrm{p}, \ \textit{if}\ 0 < d_\mathrm{n} < \widehat{d}, \\ 0, \ \textit{if}\ d_\mathrm{n} \geq \widehat{d}, \end{cases} \tag{19}$$

$$\mathbf{F}_\mathrm{t} = \begin{cases} \left(-\dfrac{d_\mathrm{t}^2}{\widehat{s}^2} + \dfrac{2|d_\mathrm{t}|}{\widehat{s}}\right)\mu_\mathrm{t}\mathbf{F}_\mathrm{n}\mathbf{t}_\mathrm{p}, \ \textit{if}\ |d_\mathrm{t}| < \widehat{s}, \\ \mu_\mathrm{t}\mathbf{F}_\mathrm{n}\mathbf{t}_\mathrm{p}, \ \textit{if}\ |d_\mathrm{t}| \geq \widehat{s}, \end{cases} \tag{20}$$

where k denotes the normal stiffness. d_n and d_t represent the normal and slip distances of two contact bodies, respectively. $\mathbf{n}_\mathrm{p}$ and $\mathbf{t}_\mathrm{p}$ are the normal and slip direction vectors of two contact bodies, respectively. $\widehat{d}$ represents the critical normal distance, where the normal contact force $\mathbf{F}_\mathrm{n}$ is activated only when the normal distance is smaller than this threshold. $\widehat{s}$ denotes the critical slip distance, beyond which the frictional force $\mathbf{F}_\mathrm{t}$ remains constant once the normal displacement exceeds $\widehat{s}$. The friction coefficient μ_t is a dimensionless material property that characterizes the resistance to sliding between two contacting surfaces.

The parameterization scheme employed in Eqs. (19) and (20) follows the theoretical framework established by Zhao et al. [61], where the critical normal distance $\widehat{d}$ is set equal to the slip threshold $\widehat{s}$. While empirical studies [60,61] often recommend setting $\widehat{d}$ between $10^{-3}L$ to $10^{-4}L$ (where L denotes the characteristic domain size) or even smaller than $10^{-4}L$ for large-scale simulations, we propose a particle-scale rationale for our resolved CFD-DEM context. We link $\widehat{d}$ directly to the particle diameter to align with explicit resolution of individual particles. Assuming an acceptable relative error of 5 %, $\widehat{d}$ is initially defined as 5 % of the particle diameter. For practical implementation, we set $\widehat{d} = 0.1\, d_\mathrm{c,min}$, where $d_\mathrm{c,min}$ is the minimum distance between contact points and adjacent particle centroids. This ensures a sufficiently small numerical threshold for robust contact resolution in particulate simulations. The normal stiffness k is then determined as $k = \left(p_\mathrm{N,0}\right)_\mathrm{optimal}/(2.256\,\widehat{d})$, consistent with the contact theory in [61]. Here, $\left(p_\mathrm{N,0}\right)_\mathrm{optimal}$ denotes the theoretical optimal initial contact force for a perfectly closed contact at the start of the simulation, which we take as the static force on a particle surface, $\left(p_\mathrm{N,0}\right)_\mathrm{optimal} = m_\mathrm{p}|\mathbf{g}|$.

Accurate computation of the normal separation distance d_n and the tangential slip displacement d_t is essential for evaluating contact forces. Using computational geometry principles, we simplify the collision detection between arbitrarily shaped triangulated solids into two fundamental interaction modes: point-face (PF) and edge-edge (EE) contacts, as depicted in Fig. 2.

For each contact mode, we rigorously derive the normal and tangential displacement components through geometric projection operations, subsequently computing the corresponding normal contact force and Coulomb friction force. The detailed numerical implementation workflow, including geometric query algorithms and force resolution procedures, is systematically outlined in

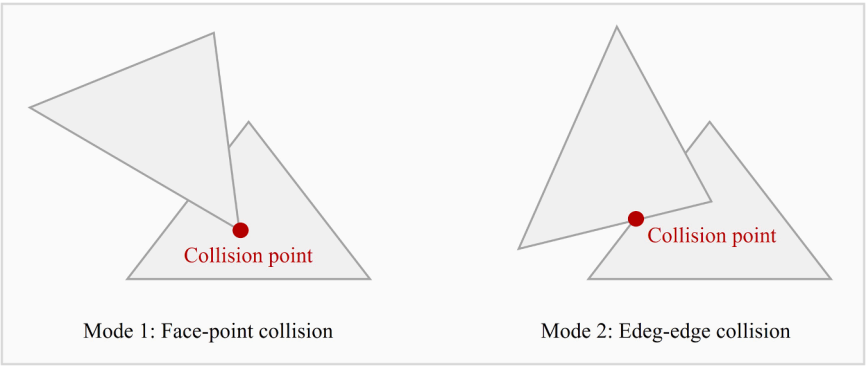

Fig. 2. Two collision modes: (1) Point-face collision; (2) Edge-edge collision.

Algorithm 1
Computational procedure of the collision model.

Steps		Treatments
1:	Obtain STL data	Store lists of vertices P_i and normal vectors $\mathbf{n}_{fi}$ of particles.
2:	Construct an edge list	Store the vertex indices corresponding to each edge of the particle.
3:	PF collision detection	Iterate through each point, search for neighboring faces of adjacent particles, and compute the normal vector $\mathbf{n}_p$ and distance d_n.
4:	PF displacement	Accumulate displacement between two particles: $\mathbf{u}+=\Delta\mathbf{u}$ if $d_n<\widehat{d}$ and $=0$if $d_n\geq\widehat{d}$.
5:	PF normal force	Compute the normal force $\mathbf{F}_n$ using Eq. (19).
6:	PF slip direction	Calculate the slip displacement vector: $\mathbf{u}_t=\mathbf{u}-(\mathbf{u}\cdot\mathbf{n}_p)\mathbf{n}_p$, and update the slip direction vector $\mathbf{t}_p=\mathbf{u}_t/\parallel\mathbf{u}_t\parallel$.
7:	PF friction force	Calculate the slip distance $d_t=\parallel\mathbf{u}_t\parallel$ and compute the corresponding friction force $\mathbf{F}_t$ using Eq. (20).
8:	EE collision detection	Iterate through each edge, search for neighboring edges of adjacent particles, and compute the normal vector $\mathbf{n}_p$ and distance d_n.
9:	EE displacement	Accumulate displacement between two particles: $\mathbf{u}+=\Delta\mathbf{u}$ if $d_n<\widehat{d}$ and $=0$if $d_n\geq\widehat{d}$.
10:	EE normal force	Compute the normal force $\mathbf{F}_n$ using Eq. (19).
11:	EE slip direction	Calculate the slip displacement vector: $\mathbf{u}_t=\mathbf{u}-(\mathbf{u}\cdot\mathbf{n}_p)\mathbf{n}_p$, and update the slip direction vector $\mathbf{t}_p=\mathbf{u}_t/\parallel\mathbf{u}_t\parallel$.
12:	EE friction force	Calculate the slip distance $d_t=\parallel\mathbf{u}_t\parallel$ and compute the corresponding friction force $\mathbf{F}_t$ using Eq. (20).
13:	Update particle motion	Sum the contact forces acting on the particle and update its motion and position using the DEM approach.

Algorithm 1.

2.3.3. *Construction of solid fraction field*

In numerical simulations involving mobile porous media, precise determination of real-time solid-phase spatial distribution within the CFD domain is critical for dynamically identifying porous regions. This study employs a coupled resolved CFD-DEM framework, where the spatial occupancy of irregular-shaped particles within individual CFD cells is quantified through a solid fraction field. To achieve high-fidelity reconstruction of this field, the signed distance field (SDF) methodology proposed by Lai et al. [34] is implemented. The SDF value D, defined as the minimum distance from each CFD mesh vertex to particle surfaces (with positive and negative values distinguishing exterior and interior regions, respectively), serves as the basis for iteratively updating the solid fraction field via Eq.(21) using an SDF-based interpolation scheme.

$$\varepsilon_p=\frac{\sum_{D<0}|D|}{\sum|D|} \tag{21}$$

Subsequently, the porosity field is reconstructed through a composite formulation:

$$\phi=\sum\varepsilon_p\phi_p+\left(1-\sum\varepsilon_p\right) \tag{22}$$

where ϕ_p denotes the intrinsic porosity of the porous particle. The porosity for cell i, is evaluated by summing over all particles that geometrically overlap with it, which ensures an accurate representation in dense regions where multiple particles may occupy a single control volume, such as in regions where two particles are in contact. This dual-component model explicitly decouples the contributions from (i) effective porosity modulated by solid-phase distribution and (ii) preserved background porosity in solid-free regions. The formulation ensures both smooth porosity transition at fluid-porous interfaces and rigorous mass conservation during solid-phase motion, addressing key challenges in multiphase porous media simulations. The integration of these methodologies within the GPU-accelerated *TFluid* platform developed by the authors enables efficient resolution of complex particle-fluid interactions while maintaining numerical stability across dynamic boundary conditions.

For geometrically regular shapes and analytically defined solids, the SDF can be directly computed using established analytical formulas. However, irregular particle morphologies, which lack predefined mathematical representations, require numerical

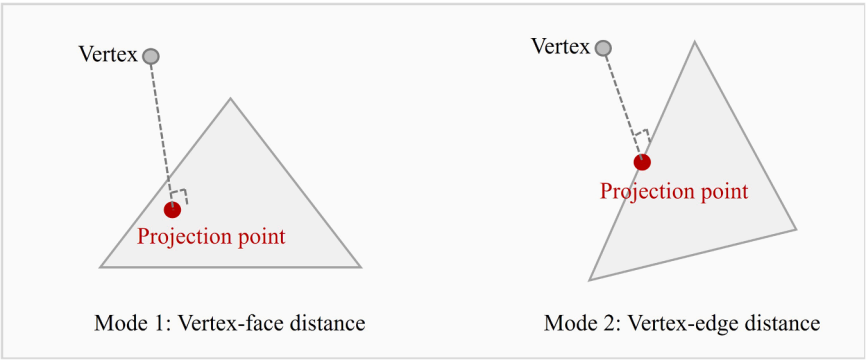

Fig. 3. Two distance modes: (1) Vertex-face distance; (2) Vertex-edge distance.

Algorithm 2
Computational procedure of the SDF computation.

Steps		Treatments
1:	Hash grid construction	Establish a cubic hash grid based on the CFD domain.
2:	Hash list generation	Store the triangular facets and edges of the particles into their corresponding hash grid cells and construct a hash list.
3:	Distance calculation	Iterate through the cell vertices, determine the hash grid cell they belong to, and search the surrounding 27 neighboring hash grid cells for triangular facets and edges. Compute the minimum distance from each cell vertex to these facets and edges.
4:	SDF computation	Compare the two types of minimum distances obtained in Step 3, and assign the shortest distance to the corresponding SDF value for the given cell vertex with respect to a specific particle.

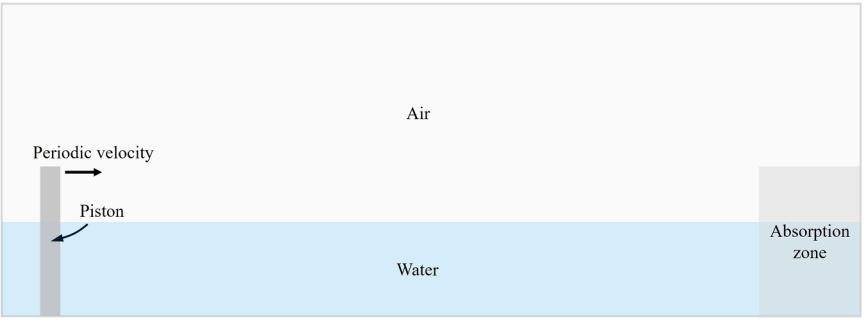

Fig. 4. Schematic of wave generation by the piston-type wave maker and the absorption zone.

approaches to determine SDF values. To address this challenge, we develop a computational framework based on spatial hashing algorithms, enabling efficient SDF calculation for arbitrarily complex geometries. Rooted in the fundamental definition of SDF, our methodology draws inspiration from collision detection paradigms by categorizing proximity computations into two distinct modes: (1) vertex-to-surface distance, defined as the shortest Euclidean distance from a mesh vertex to the particle surface, and (2) vertex-to-edge distance, representing the minimal distance between a vertex and particle edges, as schematically illustrated in Fig. 3. The final SDF value is obtained through comparative evaluation of these dual distance metrics. A complete implementation workflow of this procedure is provided in Algorithm 2. While the underlying geometric calculations employ standard vector algebra and optimization principles, their implementation details, constituting well-established procedures in computational geometry, are omitted here for brevity. This hybrid strategy effectively balances algorithmic generality with computational efficiency, particularly when handling the intricate geometric configurations characteristic of porous media systems. By integrating spatial hashing with adaptive proximity detection, the proposed method achieves robust SDF determination while maintaining scalability for large-scale particle-fluid interaction simulations.

The complete SDF computation procedure is outlined as follows:

2.4. Numerical aspects

2.4.1. Wave modulus

Wave generation, a standard technique in coastal hydrodynamics, is implemented in this study using a piston-type wavemaker,

modeled within the CFD-DEM framework via the immersed boundary method [62]. As illustrated in Fig. 4, the piston is represented as a finite-thickness rectangular plate, treated as a non-spherical rigid body fully coupled with the two-phase flow in the resolved CFD-DEM formulation. A time-dependent sinusoidal velocity is prescribed to the plate, with the resulting piston motion enforced through a localized forcing term added to the momentum equation. This approach generates waves without requiring moving meshes. Key advantages of this immersed-boundary strategy include: (1) simulation of both the piston and porous structures on a single, fixed background grid. (2) Elimination of mesh regeneration and associated interpolation errors. (3) Enhanced numerical robustness for large-scale CFD-DEM computations.

The momentum-equation source term introduced by the immersed boundary method is given as follows:

$$\mathbf{f}_{w1} = C(x) \cdot \mathbf{A}_{\mathbf{u}} \left({\mathbf{u}_f}^{n+1} - v_w \mathbf{n}_w \right) \tag{23}$$

Here, $C(x)$ is a spatially dependent coefficient, which takes the value C with $C = 1$ at the location of the piston and is zero elsewhere. The term v_w denotes the prescribed velocity of the piston, which is determined according to the desired wave profile. For instance, to generate a simple sinusoidal wave, the velocity can be defined as $v_w = A\omega\cos(\omega t)$, where A is the wave amplitude and ω is the angular frequency. $\mathbf{n}_w$ denotes the moving direction of the piston.

To complement the wave generation technique, an absorption zone is implemented at the outlet to prevent reflected waves from contaminating the generated periodic wave field. Using the source term method, a damping force is applied within the absorption zone to gradually restore the flow to a still-water state. The corresponding source term force, which is added to the right-hand side of the CFD momentum equation, is defined as follows.

$$\mathbf{f}_{w2} = \sigma_{max} \times \ 0.5 \left(1 - \cos\left(\pi \frac{x - x_1}{x_2 - x_1} \right) \right) \mathbf{A}_{\mathbf{u}} \mathbf{u}_f^{n+1} \tag{24}$$

Here, σ_{max} is a user-defined parameter that controls the damping strength within the absorption zone. The coordinates x_1 and x_2 define the spatial extent of the absorption region.

2.4.2. Numerical implementation

The finite volume method (FVM) is adopted to numerically solve the computational fluid dynamics (CFD) governing equations, encompassing the continuity equation (Eq. (1)) and momentum equation (Eq. (11)). In parallel, the discrete element method (DEM) governing equations are discretized via an explicit time integration scheme. To address the computational demands of multiphysics coupling, specifically two-phase flow, porous media interactions, and resolved CFD-DEM coupling, a fully GPU-accelerated framework is implemented. This framework, integrating porous-resolved CFD-DEM capabilities, has been deployed within the *TFluid* software (www.t-fluid.com), a CUDA C++-based platform optimized for high-performance computing. While GPU parallelization significantly enhances computational efficiency, the present study prioritizes the development of multiphysics coupling algorithms; therefore, the technical specifics of parallel implementation are beyond the scope of this discussion.

2.4.3. Numerical discretization of governing equations

The continuity and momentum equations are discretized using FVM, as formalized in Eqs. (1) and (11). The transient terms are integrated in time using a first-order Euler scheme, while the convective terms are discretized using an upwind scheme. Viscous diffusion terms are evaluated via Gauss' divergence theorem. After spatial and temporal discretization, all terms are split into implicit and explicit contributions: implicit terms are assembled into the coefficient matrix, whereas explicit terms are accumulated in the constant vector. Here, superscript n denotes the current time step (explicit terms), while $n + 1$ represents the implicit unknowns to be solved. The drag force $\mathbf{f}_d$ in Eq. (16) is partitioned into explicit and implicit components through superscript annotation. The source terms associated with wave generation and the absorption zone, as described in Section 2.4.1, are incorporated.

To couple velocity and pressure fields, the Pressure Implicit with Splitting of Operators (PISO) algorithm [63], a widely validated pressure-velocity correction method, is employed.

$${\alpha_i}^{n+1} = {\alpha_i}^n - \Delta t \cdot \sum \alpha_{if} {\varphi_f^{'}}^n - \Delta t \sum \alpha_{if} (1 - \alpha_{if}) \varphi_{cf}^n, \tag{25}$$

$$\begin{aligned} &\frac{\rho V}{\Delta t} \phi^{-1} \left(\mathbf{u}_f^{n+1} - \mathbf{u}_f^n \right) + \phi^{-1} \sum \rho {\varphi_f^{'}}^n \mathbf{u}_f^{n+1} \\ &= \phi^{-1} \sum \mu (\nabla \mathbf{u})_f^{n+1} \cdot \mathbf{n} A + \left(\mathbf{f}_c^n + \mathbf{f}_d - \nabla p + \mathbf{f}_{w1} + \mathbf{f}_{w2} \right) V, \end{aligned} \tag{26}$$

Boundary-face values are determined by their prescribed boundary conditions. For the two most common types of boundary conditions, Dirichlet (first-type) and Neumann (second-type), the boundary constraints correspond to fixed values and fixed gradients, respectively. For a boundary face *f, Dirichlet condition* specifies a fixed value at the face, e.g., $\mathbf{u}_f = \mathbf{u}_b$. The face-normal gradients are then obtained from the difference between the boundary value and the adjacent cell-center value, e.g., $\nabla \mathbf{u}_f = (\mathbf{u}_b - \mathbf{u}_c) / |\mathbf{d}|$, where $\mathbf{u}_c$ is the value at the neighboring cell center and $\mathbf{d}$ is the distance vector from the cell center to the boundary face center. *Neumann conditions* specify a fixed face-normal gradient, e.g., $\nabla \mathbf{u}_f = \nabla \mathbf{u}_b$. The face value is subsequently reconstructed as $\mathbf{u}_f = \mathbf{u}_c + \mathbf{d} \cdot \nabla \mathbf{u}_b$. Once the boundary-face values or gradients are determined, they are directly incorporated into the discretized equations, completing the finite-volume assembly of the system. This approach ensures consistency between boundary constraints and discrete operators and remains compatible with both implicit and explicit solution strategies.

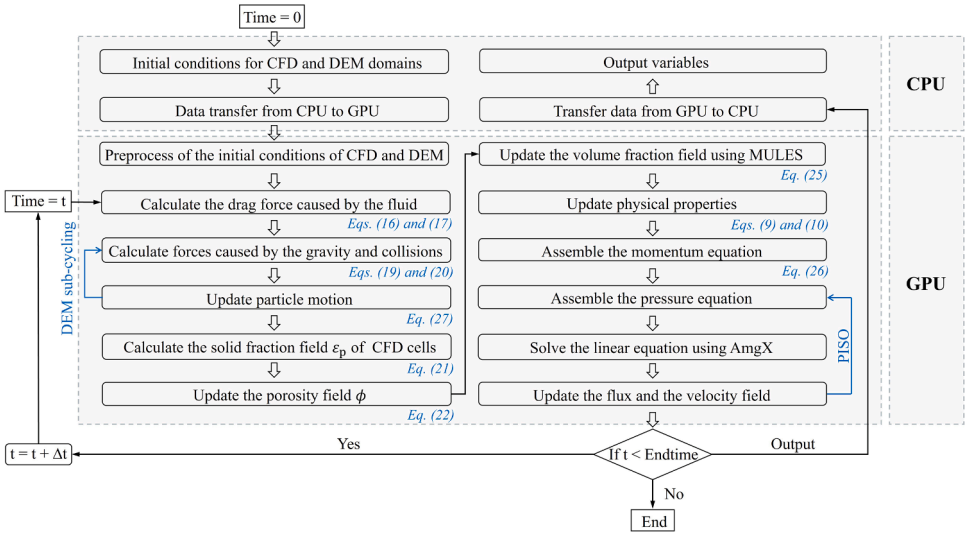

Fig. 5. Implementation flowchart of the fully GPU-accelerated porous-resolved two-phase CFD-DEM framework, where blue texts indicate governing equations for corresponding steps.

Table 1
Model setup of six benchmark cases.

Benchmark index	Basic model setup	Validation objective
I [40,64]	Stationary porous media	Capillary model, gravity, and two-phase model
II [40]		Permeability model and two-phase model
III [40,65]	Stationary porous media and pure fluid regions	Capillary model and two-phase model
IV [66,67]		Permeability model and two-phase model
V [33]	Two-dimensional moving porous structure and pure fluid regions	Permeability model, two-phase model, and resolved CFD-DEM
VI [68]	Three-dimensional moving porous structure and pure fluid regions	Permeability model, two-phase model, resolved CFD-DEM, and grid-resolution convergence test

For the DEM governing equation (Eq. (18)), an explicit temporal discretization scheme is applied, yielding Eq. (27). This approach ensures numerical stability while maintaining computational efficiency for particle-scale interactions.

$$\begin{cases} \mathbf{v}_p{}^{n+1} = \left(\mathbf{v}_p{}^{n} + \left(\mathbf{F}_f + m_p\mathbf{g} + \sum \mathbf{F}_{p-p} + \sum \mathbf{F}_{p-w}\right)^{n}\Delta t\right) \Big/ m_p \\ \omega_p{}^{n+1} = \left(\omega_p{}^{n} + \left(\mathbf{I}_p{}^{-1}\left(\sum \mathbf{M}_t + \sum \mathbf{M}_r - \omega_p \times \left(\mathbf{I}_p\omega_p\right)\right)\right)^{n}\Delta t\right) \end{cases} \tag{27}$$

2.4.4. Overall procedure

The computational framework for the full-process GPU-accelerated porous-resolved two-phase CFD-DEM method is illustrated in Fig. 5. The simulation begins with CPU-side initialization of computational domains and material properties for both the fluid (CFD) and particle (DEM) phases, followed by data transfer to the GPU for high-performance execution. The core workflow proceeds through the following major stages:

(1) Particle dynamics

Particle motions are resolved under the combined influence of fluid-induced drag (Eqs. (12) and (16)), gravity, and inter-particle contact forces (Eqs. (19) and (20)). Trajectories are updated explicitly using a time integration scheme (Eq. (27)). To maintain numerical stability under explicit integration, a DEM sub-cycling strategy is employed, whereby multiple DEM steps are performed within each CFD time step.

(2) Porous fluid coupling

The solid fraction field ε_p is reconstructed using a SDF-based algorithm (Eq. (21)). The porosity field ϕ is dynamically updated as $\phi = \sum \varepsilon_p\phi_p + \left(1 - \sum \varepsilon_p\right)$, where ϕ_p denotes particle-scale porosity and the summation includes all particles that geometrically overlap with the cell being evaluated. The volume fraction field is constrained using the MULES algorithm (Eq. (25)), while fluid properties, including the density and viscosity, are updated via Eqs. (9) and (10).

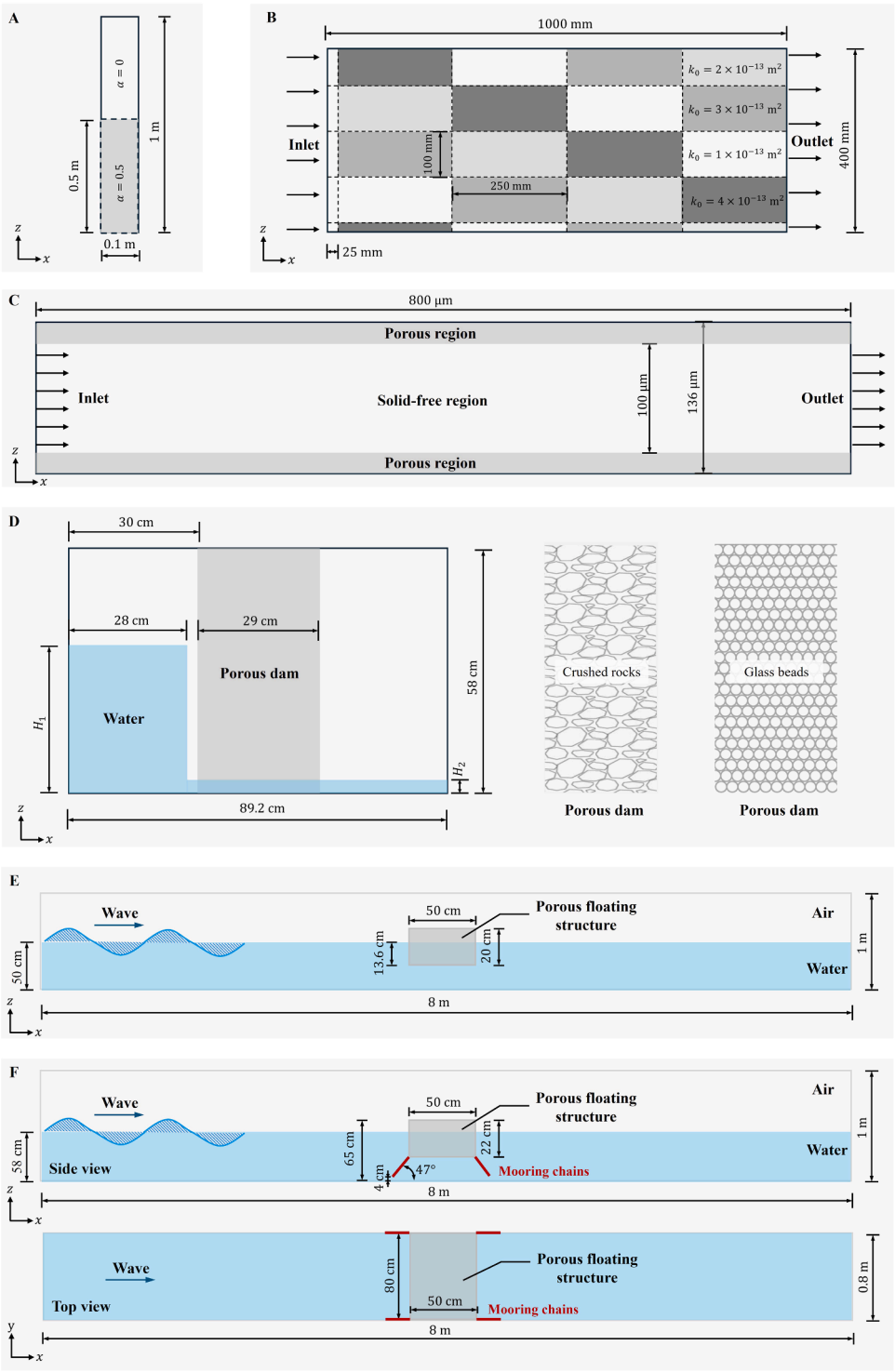

Fig. 6. . Schematic diagram of six benchmark cases. (A) Benchmark I: gravity-capillarity equilibrium [40,64]; (B) Benchmark II: oil drainage in a heterogeneous reservoir [40]; (C) Benchmark III: Taylor film [40,65]; (D) Benchmark IV: porous dam breaking [66,67]. (E) Benchmark V: two-dimensional wave-induced dynamic response of a porous structure [33]. (F) Benchmark VI: three-dimensional wave-induced dynamic response of a porous structure with mooring chains [68].

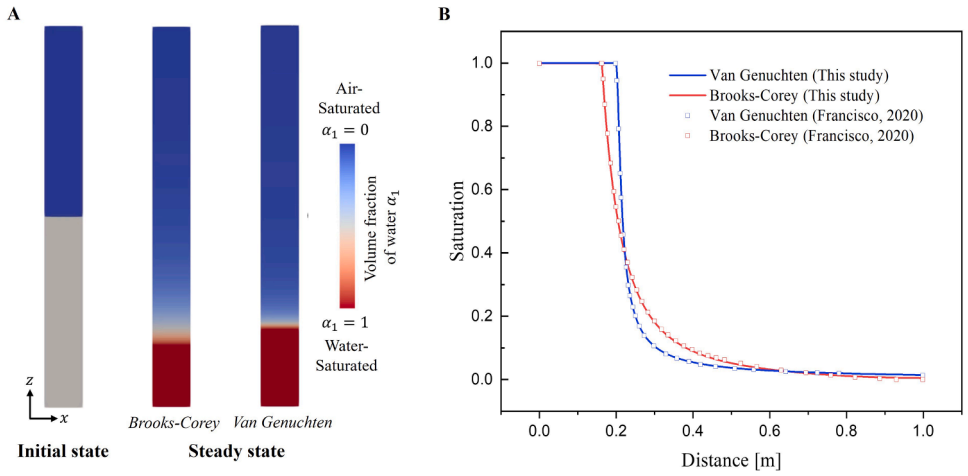

Fig. 7. (A) Initial and final water saturation profiles (volume fraction field of water) using two capillary pressure models (Brooks-Corey model and van Genuchten model). (B) Comparison of steady-state profiles from simulation results and analytical solutions [40].

(3) Fluid phase resolution
The momentum equations (Eq. (26)) is discretized with porosity-dependent terms and solved using the AmgX GPU-accelerated algebraic multigrid solver. The PISO algorithm is employed to iteratively update the velocity, pressure, and flux fields.

(4) Data management and output
Upon convergence, results are transferred back to the CPU for output processing. Termination criteria are evaluated at each iteration cycle (as indicated by decision nodes in Fig. 5).

Key equations associated with each stage are highlighted in blue texts to facilitate traceability between computational steps and their governing formulations. This tightly integrated GPU-parallelized workflow achieves high efficiency while preserving numerical stability in simulating complex fluid-porous particle interactions.

3. Benchmark and validation

In this chapter, six benchmark cases are presented to verify the performance of the proposed resolved CFD-DEM framework for multiphase flow in porous media. The cases are arranged in order of increasing complexity: (1) stationary domains composed entirely of porous media; (2) mixed domains combining stationary porous regions with pure fluid regions; and (3) mixed domains involving freely moving porous structures interacting with surrounding two-phase flows.

3.1. Model setup of six benchmark cases

To evaluate the accuracy and robustness of the proposed resolved CFD-DEM framework for multiphase flow in porous media, six benchmark cases of increasing complexity are considered. These benchmarks span a range of physical phenomena and geometrical configurations, as summarized in Table 1. The schematic diagram of six benchmark cases is shown in Fig. 6. It should be noted that, except for Benchmark II, the second fluid phase in all other benchmark cases is air, with a density of 1 kg/m^3 and a dynamic viscosity of 1.76×10^{-5} Pa·s. The primary fluid phase is water, with a density of 1000 kg/m^3 and a dynamic viscosity of 0.001 Pa·s.

- **Benchmark I** (Fig. 6A) examines the balance between gravitational and capillary forces in a one-dimensional, vertical porous column partially saturated with water and air [40,64]. The domain is 1 m tall and discretized with 1500 cells, with porosity $\phi = 0.5$ and intrinsic permeability $k_0 = 1 \times 10^{-11}$ m^2. Initially, the bottom half of the column is partially saturated (volume fraction of water $\alpha_1 = 0.5$), while the top half is dry. Both air and water are permitted to flow freely through the top boundary, while the bottom boundary is sealed. The entry capillary pressure is set to $p_{c,0} = 100$ Pa. For the van Genuchten model, the parameter $m = 0.5$, while for the Brooks-Corey model, the parameters are $m = 3$ and $\beta = 0.5$.
- **Benchmark II** (Fig. 6B) evaluates the performance of the two-phase flow model in a spatially heterogeneous porous medium representative of Darcy-scale oil reservoirs [40]. The simulation domain measures 1 m × 0.4 m and is discretized with a 2000 × 800 grid. Water is injected into an oil-saturated medium at a constant velocity of 1×10^{-4} m/s, with the outlet pressure fixed at 0 Pa. The domain's permeability is initialized as a grid of 0.25 × 0.1 m blocks, with local values ranging from 1×10^{-13} to 4×10^{-13} m^2, mimicking geological heterogeneity. Relative permeability is modeled using the van Genuchten formulation (Eqs. (7) and (9)), with the entry capillary pressure $p_{c,0} = 100$ Pa and model parameter $m = 0.5$; capillary effects are otherwise neglected in the flow field.

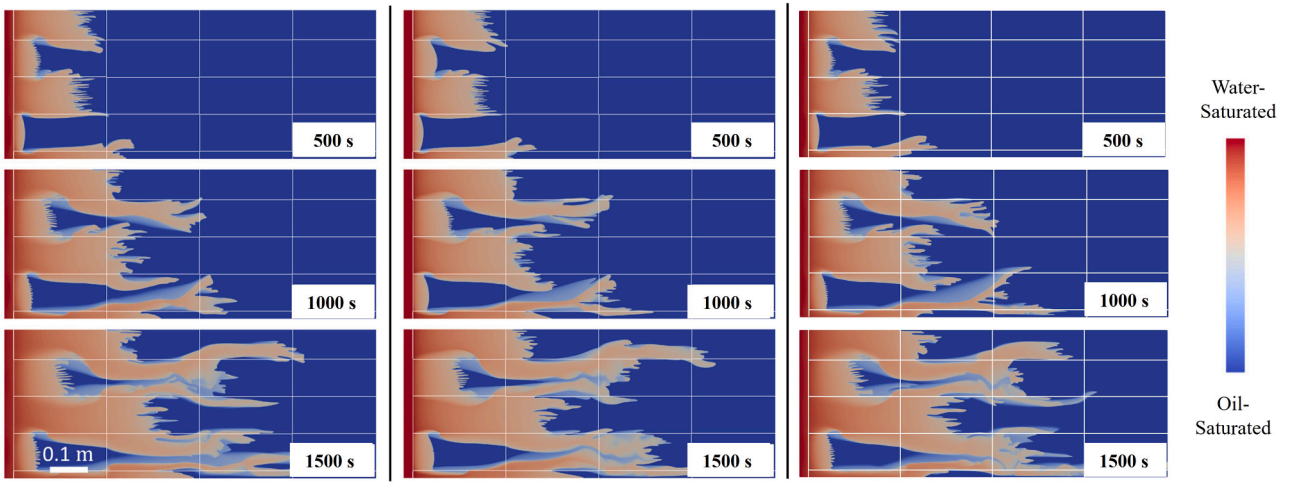

Fig. 8. Comparison of simulation results for oil drainage in a heterogeneous porous medium using different Solvers: *hybridPorousInterFoam* [40], *impesFoam* [69], and *TFluid* (this study). White grid blocks represent various permeability values, as shown in Fig. 6B.

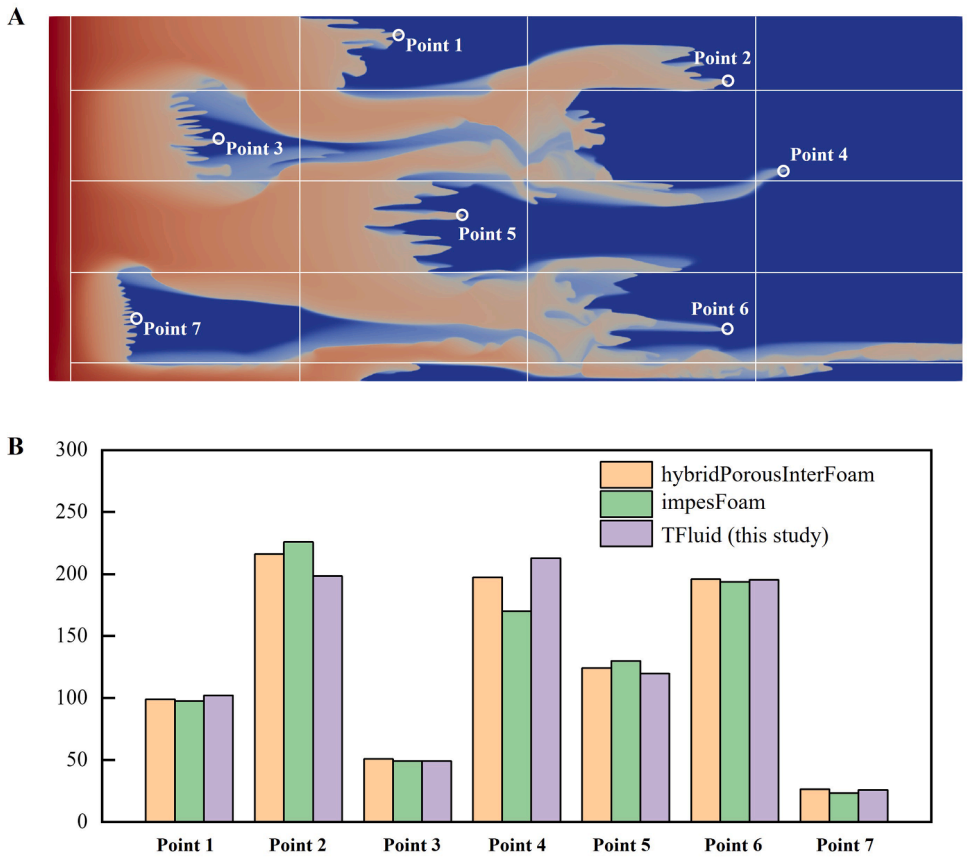

Fig. 9. (A) Locations of seven probe points placed at the leading edge of the fingering front for quantitative comparison. (B) *x*-coordinate positions of these probe points at t = 1500 s for oil drainage in a heterogeneous porous medium, as predicted by different solvers: *hybridPorousInterFoam* [40], *impesFoam* [69], and *TFluid* (this study).

- **Benchmark III** (Fig. 6C) focuses on validating the multiphase contact dynamics in a hybrid domain composed of both porous and pure fluid regions [40,65]. The system consists of a two-dimensional micro-channel measuring 800 μm in length and 136 μm in height, discretized with a 280 × 158 grid. The top and bottom 18 μm layers are modeled as porous media with permeability $k_0 = 1 \times 10^{-20}$ m^2, while the central 100 μm region represents a pure fluid zone. Ethanol, with viscosity $\mu_1 = 1.2 \times 10^{-3}$ Pa·s, density $\rho_1 = 789$ kg/m^3, and surface tension coefficient $\sigma = 0.02$ N/m, is injected from the left inlet at a velocity of 0.4 m/s. The outlet, located on the right boundary, is maintained at a fixed pressure of 0 Pa. A contact angle of 20° is imposed at the fluid-solid interface. For the permeability model, the Brooks-Corey model is employed in this case, with the model parameter set to $m = 3$. Under these conditions, a thin film forms along the channel walls due to the interplay between viscous forces and capillarity at the contact line.
- **Benchmark IV** (Fig. 6D) replicates the dam-break experiment conducted by Lin [67], in which a 29 cm-long porous dam was positioned at the center of a water tank (89.2 × 44 × 58 cm). A gate located 2 cm upstream of the dam was manually removed within 0.1 s to initiate the flow. Two types of porous materials were tested: crushed rocks (porosity = 0.49) and uniform glass beads (porosity = 0.39). The initial upstream and downstream water levels were denoted as H_1 and H_2, respectively, with $H_1 = 24$ cm and $H_2 = 2.5$ cm for the crushed rock case, and $H_1 = 25$ cm and $H_2 = 1.5$ cm for the glass bead case [66]. To reduce computational cost while retaining the key flow features, the domain was simplified to a quasi-two-dimensional setup by reducing the spanwise thickness to 4 cm, and the mesh was discretized into 178 × 8 × 120 cells. The van Genuchten model was employed to describe capillary behavior, and simulations were conducted with varying intrinsic permeabilities and model parameters to evaluate the method's sensitivity.
- **Benchmark V** (Fig. 6E) investigates the two-phase interaction between surface waves and a freely movable porous structure using a resolved CFD-DEM framework [33]. The setup replicates a two-dimensional wave flume experiment in which a porous box, representing a floating breakwater, is placed in a numerical wave tank. Following Dong's simulation setup [33], the computational domain length was set to 8 m to reduce the computational cost. A uniform grid was employed, with a cell size of 6.7 mm. The box has dimensions of 50 cm × 20 cm, a material density of 680 kg/m^3, and is freely floating without mooring constraints. Incident sinusoidal waves with an amplitude of 1.5 cm and a period of 1.2 s propagate through a still water depth of 50 cm. To establish hydrostatic equilibrium prior to wave interaction, the buoyancy force acting on the structure is evaluated, resulting in a static equilibrium draft (immersed depth) of approximately 13.6 cm. The Darcy-Forchheimer model is applied, with the drag coefficients

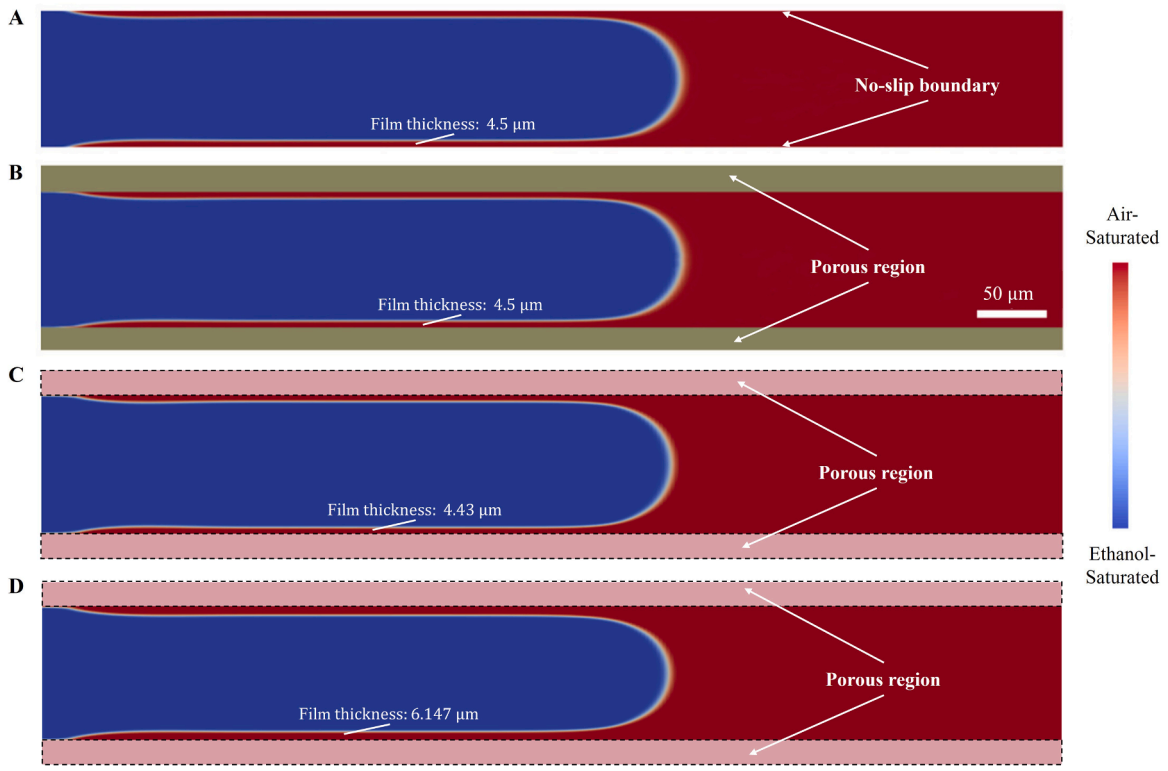

Fig. 10. Comparison of simulation results for the Taylor film case: (A) wall boundary condition using *interFoam* [40]; (B) porous region as boundary using *hybridPorousInterFoam* [40]; (C and D) porous region as boundary using the method proposed in this study with $\sigma = 0.02$ **N/m** (C) and $\sigma = 0.01$ **N/m** (D).

set to $C_{d1} = 1 \times 10^7$ m^{-2} and $C_{d2} = 37.5$ m^{-1}. This benchmark primarily validates the ability of the proposed framework to capture wave-induced motions, porous damping, and complex fluid-structure interactions in two-phase environments.

- **Benchmark VI** (Fig. 6F) builds upon Benchmark V by introducing mooring-chain constraints in a 3D wave flume, following the setup of Luo et al. [68]. The computational domain measures 8 m (length) × 0.8 m (width) × 1 m (height). A porous box (50 cm × 80 cm × 22 cm, density 680 kg/m^3) is moored by four mooring chains. Each chain is anchored 4 cm above the tank bottom (at the top of the deadweights) and attached to a bottom corner of the structure, forming an inclination angle of approximately 47° In the simulation, the chains are modeled as tension-only springs with a stiffness of 1×10^{10} N/m to provide realistic constraint. Monochromatic incident waves (height: 7.95 cm, period: 1.3 s) propagate over a still water depth of 58 cm. The porous media employs the same Darcy-Forchheimer model parameter as in Benchmark V. The baseline simulation employs a uniform 16 mm grid, with 10 mm and 25.6 mm grids used for a convergence study; the finest mesh contains 6.4 million cells. This benchmark comprehensively evaluates the capability of the proposed framework to capture wave-induced motions, porous damping, mooring dynamics, and complex fluid-structure interactions in a two-phase environment.

3.2. Benchmarking analyses

3.2.1. Benchmarks I and II: stationary porous media

The accuracy of the proposed model in capturing capillarity-driven flow behavior was first verified through Benchmark I, as shown in Fig. 7. The system evolves toward a steady-state saturation profile governed by gravity-capillarity equilibrium, wherein gravity drives the heavier water downward and capillary forces act upward. This case is used to verify the implementation and accuracy of the capillary pressure term under static equilibrium conditions. Panel (A) illustrates the initial and final water saturation profiles under two different capillary pressure models, while Panel (B) compares the simulated steady-state saturation distribution against the analytical gravity-capillarity equilibrium solution (Eq. (28)) [69]. Excellent agreement is observed in both cases, demonstrating the model's capability to resolve the interplay between gravitational and capillary forces in unsaturated porous media.

$$\frac{\partial \alpha_1}{\partial z} = \frac{(\rho_2 - \rho_1) g_z}{\frac{\partial p_c}{\partial \alpha_1}}, \tag{28}$$

where α_1 denotes the volume fraction of water, p_c is the capillary pressure computed from Eqs. (3) and (4), ρ_1 and ρ_2 represent the densities of water and air, respectively, and g_z is the gravitational acceleration in the z-direction.

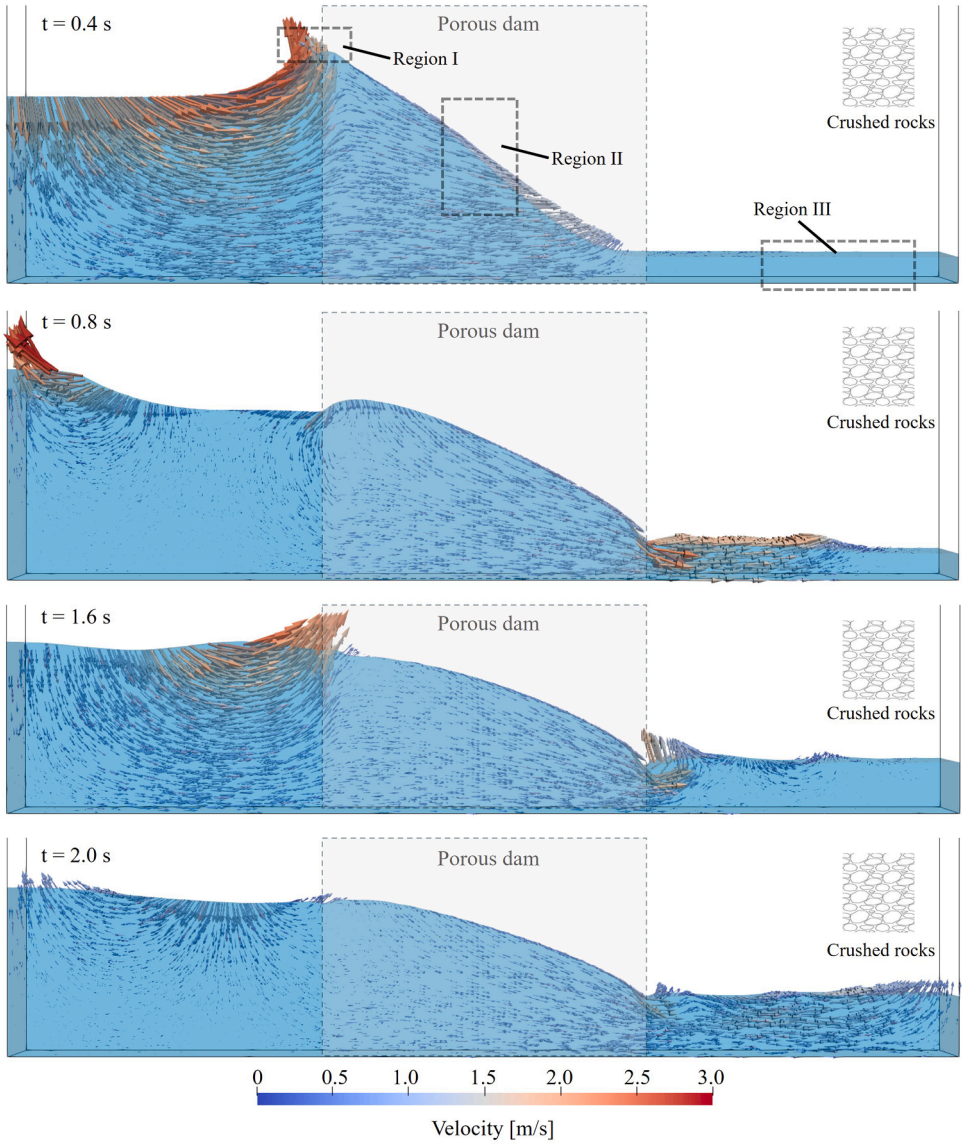

Fig. 11. Simulation results of water distribution and velocity vectors during flow through the crushed-stone dam at 0.4 s, 0.8 s, 1.6 s, and 2.0 s. The absolute permeability is $k_0 = 1.5 \times 10^{-8}$ m^2 and the van Genuchten model parameter $m = 0.8$.

Benchmark II further evaluates the model's robustness in heterogeneous reservoirs, where spatially varying permeability significantly influences two-phase dynamics. A key feature in such systems is the occurrence of viscous fingering, unstable and finger-like displacement patterns that emerge when a less viscous fluid displaces a more viscous one in a heterogeneous porous medium. These instabilities are highly sensitive to local permeability contrasts and saturation-dependent flow properties. As shown in Fig. 8, the oil drainage simulation results using the proposed solver closely match those obtained from established solvers, such as *hybridPorousInterFoam* [40] and *impesFoam* [69]. To quantify the agreement among different solvers, we have further selected seven probe points located at the tips of the dominant fingering structures (Fig. 9A). Fig. 9B presents a quantitative comparison of the x-coordinates of these seven points at $t = 1500$ s. The root mean square errors (RMSE) of the penetration distances between this study and the two reference solvers are 9.9 μm and 21.4 μm, corresponding to 0.99 % and 2.14 % of the computational domain length in the flow direction, respectively. It confirms the model's applicability to complex Darcy-scale systems with strong heterogeneity and fingering-prone displacement fronts.

3.2.2. Benchmarks III and IV: stationary porous media and pure fluid regions

Benchmark III focuses on modeling the displacement of a viscous fluid (ethanol) by air within a microchannel, a classical configuration known for producing a "Taylor film" along the channel walls [65]. This phenomenon occurs due to the competition between viscous and capillary forces at the fluid-solid interface, resulting in the formation of a thin liquid film that remains attached to

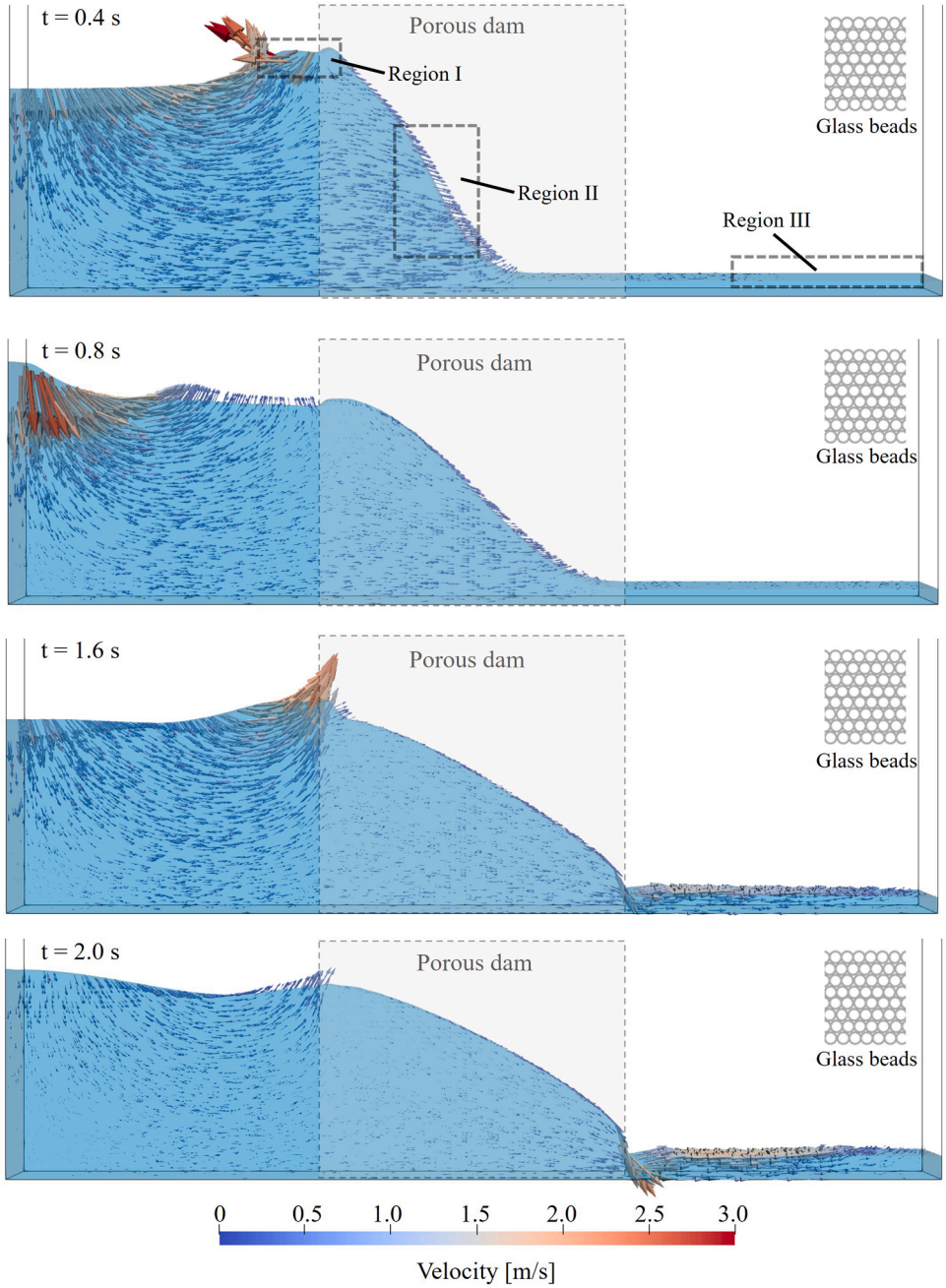

Fig. 12. Simulation results of water distribution and velocity vectors during flow through the glass-beads dam at 0.4 s, 0.8 s, 1.6 s, and 2.0 s. The absolute permeability is $k_0 = 5 \times 10^{-9}$ m^2 and the van Genuchten model parameter $m = 0.8$.

the walls as the displacing air phase advances. This benchmark is particularly useful for validating the accuracy of two-phase interface tracking, wall-film formation, and the implementation of surface tension effects within the numerical framework. The height of this film is given by the following analytical solution (Eq. (29)) [65], which we use as a benchmark to verify our numerical simulations.

$$\frac{h}{H} = \frac{1.34\mathrm{Ca}^{2/3}}{1 + 3.35\mathrm{Ca}^{2/3}}, \tag{29}$$

where h is the film thickness, H is the channel height, and Ca is the capillary number, defined as $\mathrm{Ca} = \mu_{\mathrm{ethanol}} U/\sigma$, where μ_{ethanol} is the dynamic viscosity of ethanol, U is the injection velocity, and σ is the surface tension coefficient.

The theoretical film thickness derived from analytical solutions under simulated conditions is 4.35 μm. As illustrated in Fig. 10,

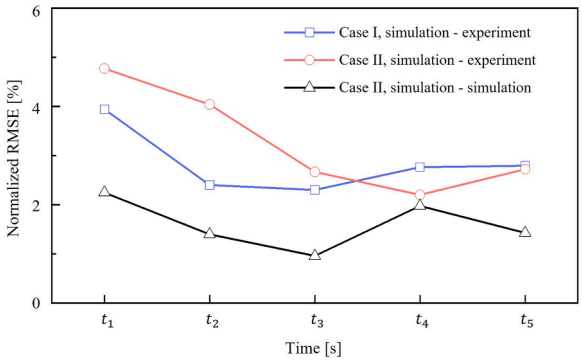

Fig. 13. Normalized root mean square errors (the ratio of RMSE to initial water column height) at different time instances for Case I and Case II, computed by comparing the current simulation results with experimental measurements [67] and previously published CFD-DEM simulation data [66]. Specifically, the RMSE is calculated using the z-coordinates of 80 uniformly distributed sampling points along the free surface. For Case I, the simulation uses $k_0 = 1.5 \times 10^{-8}$ m^2 and the time steps t_1 to t_5 correspond to 0.4 s, 0.8 s, 1.2 s, 1.6 s, and 2.0 s; for Case II, the simulation uses $k_0 = 5 \times 10^{-9}$ m^2 and t_1 to t_5 correspond to 0.4 s, 0.8 s, 1.2 s, 1.6 s, and 4.0 s.

numerical implementations using three distinct computational approaches exhibit consistent agreement with this theoretical baseline: *hybridPorousInterFoam* simulations with impermeable porous boundaries yield 4.50 μm (3.4 % deviation), while conventional *interFoam* simulations with wall boundaries produce equivalent results (4.50 μm, 3.4 % deviation). Simulations employing the revised boundary conditions resulted in 4.43 μm (1.8 % deviation), within established experimental uncertainty margins [70,71]. Further extending to reduced surface tension conditions ($\sigma = 0.01$ N/m), the theoretical film thickness measures 6.15 μm. The present algorithm achieves remarkable agreement (6.147 μm, Fig. 10D), corresponding to an exceptionally small error of 0.05 %. This quantitative consistency across methodologies, spanning wall-boundary, porous-boundary, and variable surface tension conditions, confirms the physical validity of thin-film modeling frameworks in porous media applications. The sub-percent deviation at lower surface tension further demonstrates the method's robustness in capturing capillarity-dominated regimes.

Benchmark IV evaluates the framework's ability to simulate transient two-phase flow through porous media under dam-break conditions. Figs. 11 and 12 illustrate the water infiltration process through the porous dam composed of crushed rock (Case I) and glass beads (Case II), respectively. In each figure, three representative regions are marked for detailed analysis: Region I corresponds to the cross-section where water first contacts the porous dam, Region II indicates the water level inside the dam, and Region III represents the water level at the downstream outlet. Differences in intrinsic permeability lead to distinct flow characteristics in these regions: (1) Upon initial impact, low-permeability media result in faster formation of a reflected wave in Region I, as seen in the 0.4 s snapshot of Case II; (2) Steeper water level gradients develop within the lower-permeability dam, delaying full infiltration. Complete penetration occurs around 0.8 s in Case I, while in Case II it takes approximately 1.6 s; (3) In the higher-permeability Case I, Region III exhibits a rapid rise in water level accompanied by noticeable wave formation, whereas in Case II, the water level in Region III increases slowly and remains smooth. Such insights into localized flow behaviors and permeability effects can inform the future design and optimization of porous dams and embankments in hydraulic engineering applications, particularly where selective infiltration and controlled drainage are critical.

To assess the accuracy of the proposed method, Figs. 13–18 present a quantitative comparison of the simulated free-surface profiles for Case I and Case II with experimental data [67] and CFD-DEM simulation results [66]. Since the experiments do not provide absolute permeabilities, permeability values were selected through testing to match the experimental observations. The comparisons (Figs. 14–18) demonstrate excellent agreement between the present simulations, the experimental observations, and the CFD-DEM results, accurately capturing the evolution of the free surface on both sides of the dam, the water level at the dam interface, and the internal seepage profile within the porous medium. To further quantify the agreement, 80 uniformly distributed points were selected along the free-surface profiles in the x-direction, and RMSE of the z-direction coordinate were calculated. As shown in Fig. 13, the RMSE values between the current simulation results, experimental measurements, and previously published simulation data were evaluated for both Case I and Case II across five different time instances. The maximum RMSEs were 0.95 cm, 1.15 cm, and 0.54 cm, corresponding to 3.95 %, 4.6 %, and 2.16 % of the initial water column height, respectively. The average RMSEs over the five timesteps were 0.68 cm, 0.79 cm, and 0.38 cm, which represent 2.83 %, 3.16 %, and 1.52 % of the initial water height. Two factors contribute to the observed discrepancies. First, the continuum approach uses an empirical permeability model that may not fully represent the pore-scale geometry of the experimental granular packing. Second, the numerical simulation assumes an instantaneous release, unlike the finite gate-opening duration (around 0.1 s) in the experiment [67]. Nevertheless, the overall errors remain within an acceptable margin, as evidenced by a mean deviation of only 1.5 %. These results highlight the proposed model's ability to accurately capture permeability-dependent flow transitions and surface dynamics in porous structures under highly transient conditions.

Although minor discrepancies are observed between the current simulation and the experiment in certain details, such as the free surface at the right dam interface at 0.4 s for both Case I and Case II (see Figs. 14 and 16), our results align very closely with those from the CFD-DEM simulations in these regions. This explains why the largest RMSE consistently occurs at the initial time point ($t_1 = 0.4$ s) in Fig. 13. These differences can be attributed to two primary factors: (1) In the experiments, the flow was initiated by manually

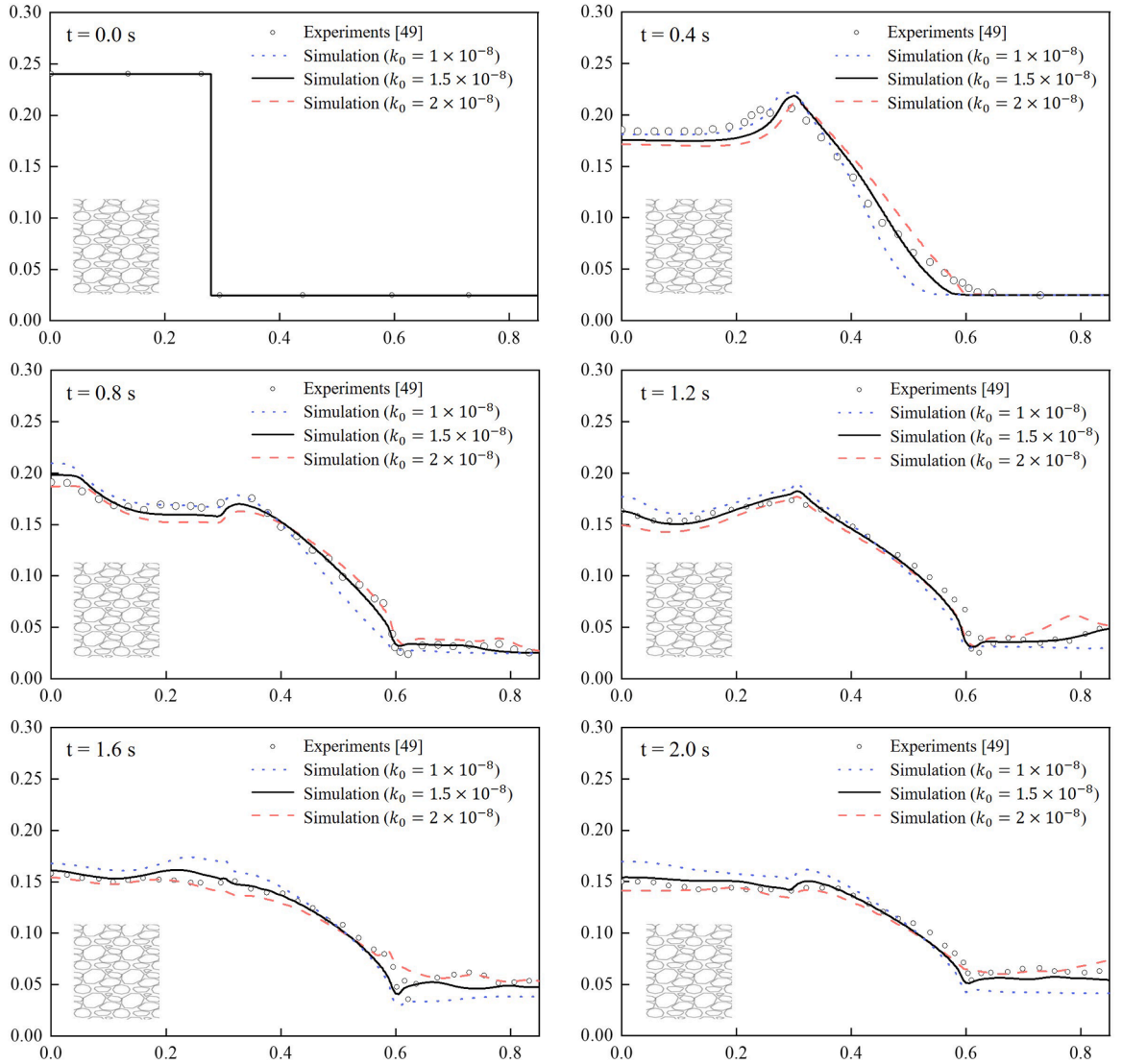

Fig. 14. Comparison of simulation results with the absolute permeability $k_0 = 1 \times 10^{-8}$, 1.5×10^{-8}, and 2×10^{-8} m^2 against experimental testing data [67] for flow through the crushed-stone dam.

removing a gate over approximately 0.1 s, which introduces a slightly different initial condition compared to the simulations where the water column collapses instantaneously; (2) The porous dam in the simulation was modeled as a homogeneous and isotropic porous medium for simplicity, whereas the actual experimental structure inevitably exhibits certain heterogeneities.

To examine the effects of absolute permeability and model parameters on the simulation outcomes, a series of comparative simulations were conducted with varying input values. Figs. 14 and 15 compare the results of Case I under different absolute permeability values and model parameters, while Figs. 16 and 17 present the corresponding comparisons for Case II. The results show that the model parameter has a negligible influence on the free surface profile, whereas absolute permeability plays a dominant role. As the absolute permeability increases, the infiltration rate accelerates significantly, resulting in a more rapid drop in the upstream water level and a faster rise in the downstream free surface. This is also accompanied by more pronounced wave motions, as observed at 1.2 s in Fig. 15. These findings are consistent with the earlier comparisons between the crushed-stone dam and the glass-beads dam.

3.2.3. Benchmark V: two-dimensional moving porous structure and pure fluid regions

Benchmark V investigates the coupled interaction between a freely moving porous structure and two-phase flow (waves), extending the previous benchmarks involving static porous structures. This case further validates the capability of the fully resolved CFD-DEM framework and the proposed porous media model in handling fluid-structure interaction. Fig. 19 compares the experimental [33] and simulated responses of the porous structure over one wave period, including its dynamic posture and the trajectory of the center of gravity (CoG). The results show that our simulation can accurately reproduce both the motion posture of the porous structure and the

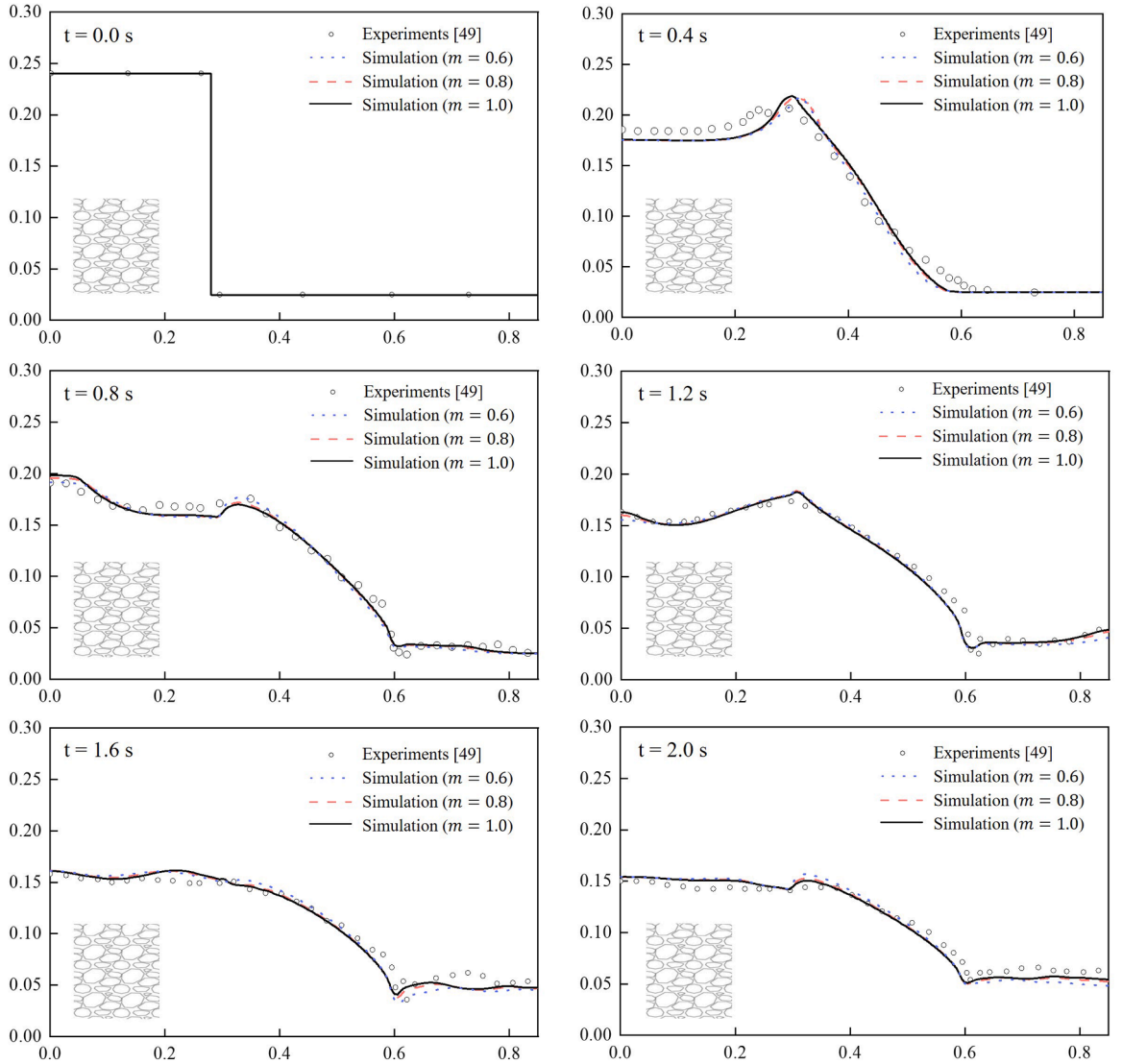

Fig. 15. Comparison of simulation results with the van Genuchten model parameter $m = 0.6$, 0.8, and 1.0 against lexperimental testing data [67] for flow through the crushed-stone dam.

free surface profiles on both sides, consistent with experimental observations. To further elucidate the mechanisms behind the structure's motion, Fig. 19C presents velocity vector fields of the flow inside and around the porous body. Notably, the fluid within the porous structure exhibits higher velocities than the surrounding fluid, which can be attributed to the dynamic interaction induced by the motion of the structure itself. We will analyze this velocity field in more detail later when comparing the dynamics of the porous structure (Fig. 22) with those of an enclosed structure.

Fig. 20A depicts the CoG trajectories obtained from the experiment [33], previous simulations [33], and the current study. The results demonstrate that the CoG trajectory predicted by the present method closely follows the trend of previous simulations and provides more accurate estimates of single-period displacements in both the x and z directions. Compared with the experimental mean displacements over three wave periods (0.0615 m in x and 0.0368 m in z), the current simulation yields values of 0.0626 m and 0.0358 m, corresponding to relative errors of only 1.8 % and 2.37 %, respectively. In contrast, the previous simulation results showed displacements of 0.0601 m and 0.0355 m, with errors of 2.3 % and 3.53 % [33]. These results further confirm the accuracy of the proposed method in simulating the dynamics of freely floating porous structures.

While the simulated x- and z-direction displacements agree closely with experiments, the trajectory shape diverges slightly at the start of each wave period. This discrepancy stems from an assumption in the current numerical approach, which homogenizes the discrete porous structure into a continuum material with uniform porosity and permeability. In contrast, the experiment uses discretely arranged spheres in a stratified configuration for the porous structure [33], creating preferential flow channels. These channels allow early fluid passage upon wave impact, reducing the initial force on the structure and altering the trajectory slope, an effect our

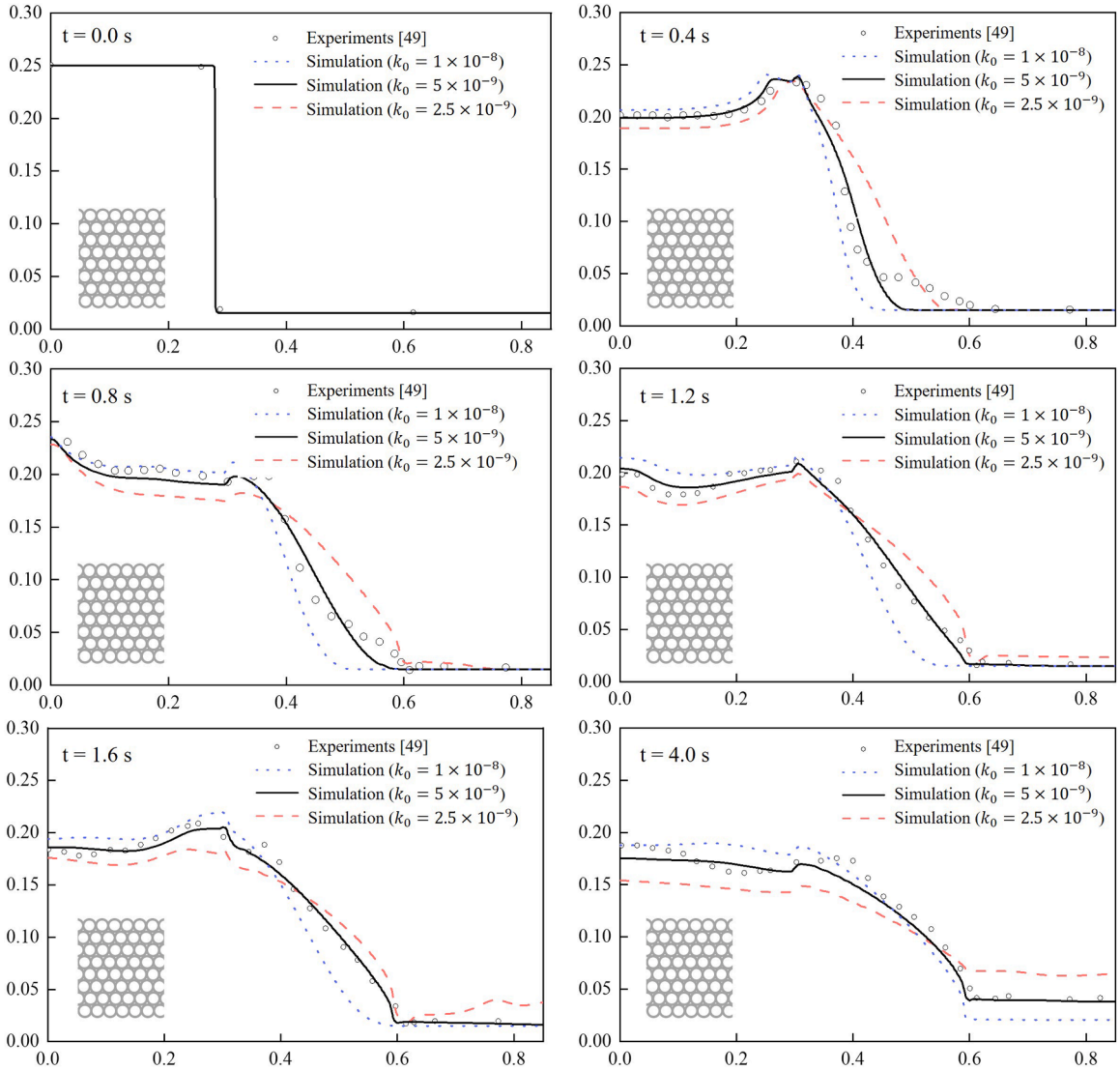

Fig. 16. Comparison of simulation results with the absolute permeability $k_0 = 1 \times 10^{-8}$, 5×10^{-9}, and 2.5×10^{-9} m^2 against experimental testing data [67] for flow through the glass-beads dam.

homogenized model largely smoothed over. Nevertheless, the overall trajectory pattern aligns with prior continuum-based numerical studies [33]. A more detailed mechanistic analysis would necessitate comparison with fully discrete models.

We replaced the porous structure with an enclosed structure of identical shape and density to further investigate the motion behavior of a closed body under wave action, and to analyze the differences in dynamic response between the two configurations, along with the underlying physical mechanisms. Fig. 20B presents the trajectories of the CoG for both the porous and enclosed structures, while Fig. 22 illustrates the motion and surrounding flow velocity vectors of the enclosed structure over a single wave period. The results clearly reveal distinct differences between the two types of structures. The porous structure exhibits a significantly longer trajectory within a single period, approximately 1.67 times that of the enclosed structure. In terms of shape, the CoG trajectory of the porous structure resembles a half-ellipse within a single period, while that of the enclosed structure forms a nearly complete ellipse with a noticeable overlap between successive periods. Both structures exhibit similar vertical (z-direction) displacements, primarily determined by the wave amplitude. However, their draft depths differ due to buoyancy effects: the porous structure sits deeper in the water than the enclosed structure, as shown in Figs. 19 and 22.

Fig. 21 presents comparative profiles of x-direction linear velocity and angular velocity magnitude for porous and enclosed structures under wave loading, with z-direction velocities omitted due to negligible inter-structural differences. Both velocity components exhibit periodic oscillations precisely synchronized with the 1.2 s wave period. Critically, the porous structure demonstrates significantly amplified x-direction linear velocities, where positive and negative peaks exceed those of the enclosed configuration by 0.01 m/s and 0.022 m/s respectively, yielding a mean cycle differential of 0.033 m/s. This translational enhancement facilitates

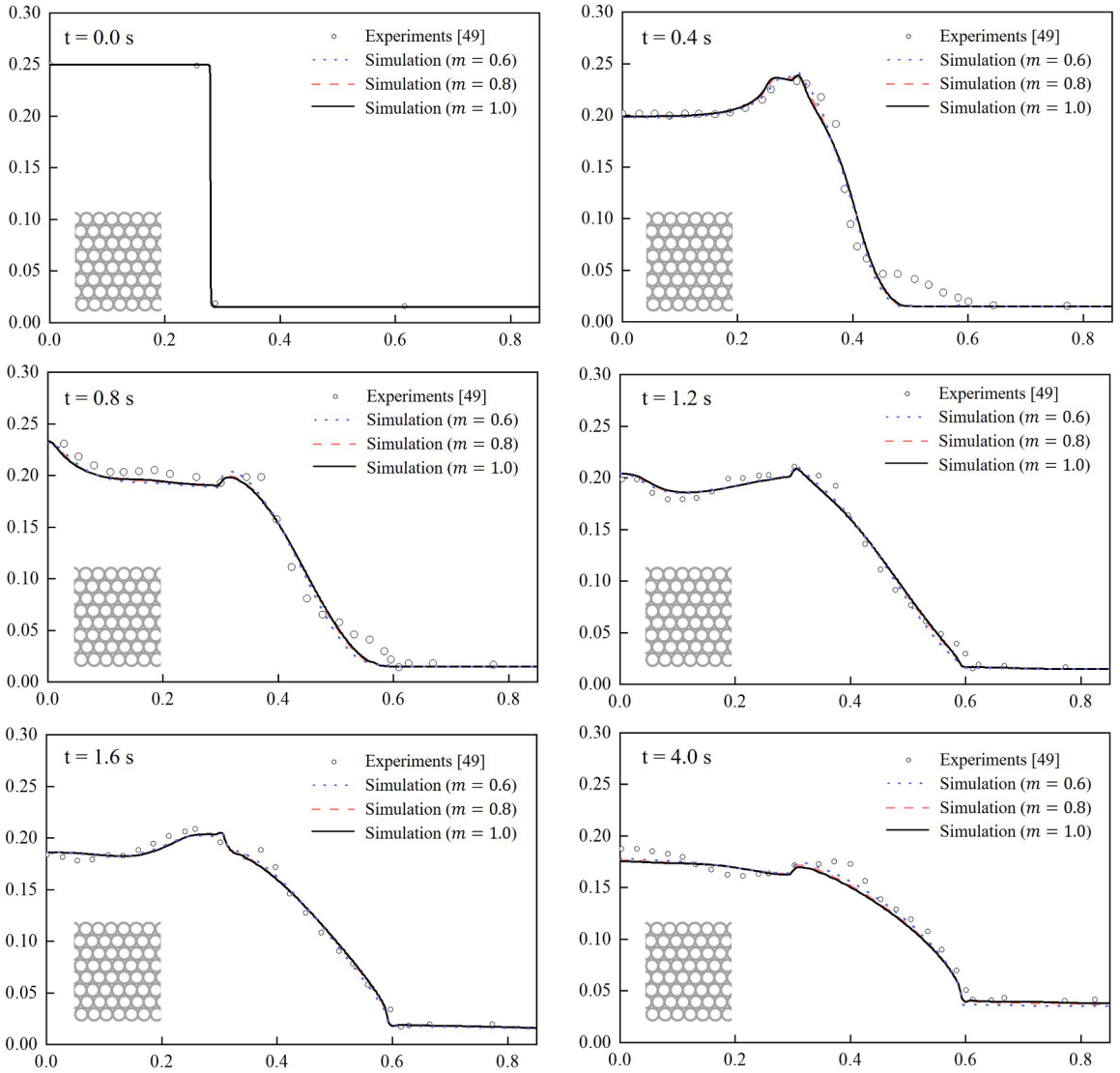

Fig. 17. Comparison of simulation results with the van Genuchten model parameter $m = 0.6$, 0.8, and 1.0 against experimental testing data [67] for flow through the glass-beads dam.

greater positive displacement in porous systems, mechanistically explaining their characteristic tilted elliptical trajectory observed in companion analyses (Fig. 20B). Conversely, angular velocity profiles show closely matched oscillation patterns with near-symmetric peaks, though enclosed structures exhibit stronger rotational response with peak magnitudes exceeding porous values by approximately 0.09 rad/s, indicating more pronounced rotational oscillations under wave excitation. The dichotomy arises from interstitial fluid penetration augmenting translational momentum in porous media versus wave energy concentration in rotational modes for enclosed systems due to restricted permeability.

To further explore the differences in horizontal (x-direction) motion, a comparison between Figs. 19 and 22 highlights a key observation: a strong vortex appears in the forward region of the porous structure, where the free surface consistently moves rightward at all six time points across the wave cycle. This persistent rightward motion drives the formation of a localized vortex. In contrast, for the enclosed structure, free surface motion near the front is primarily governed by wave phase, showing more symmetric oscillations. For example, at T/6 and 2T/6 in Fig. 21, fluid on the right side of the enclosed structure moves leftward, opposing its motion and generating resistance. This contrast is absent in the porous case because the incoming wave crest propagates through the porous structure and continues to the lee side, as seen from T/6 to 2T/6 in Fig. 19. Due to drag effects, part of the wave energy is transferred into kinetic energy of the porous body, causing it to oscillate while drifting in the direction of wave propagation. The fluid that passes through the porous medium interacts with the surrounding flow, generating vortices that mitigate the opposing force in front of the structure, thereby facilitating its net forward motion. Overall, the porous structure demonstrates a superior capacity to dissipate wave energy by transforming a larger share of the incoming wave energy into kinetic motion, highlighting its potential effectiveness in

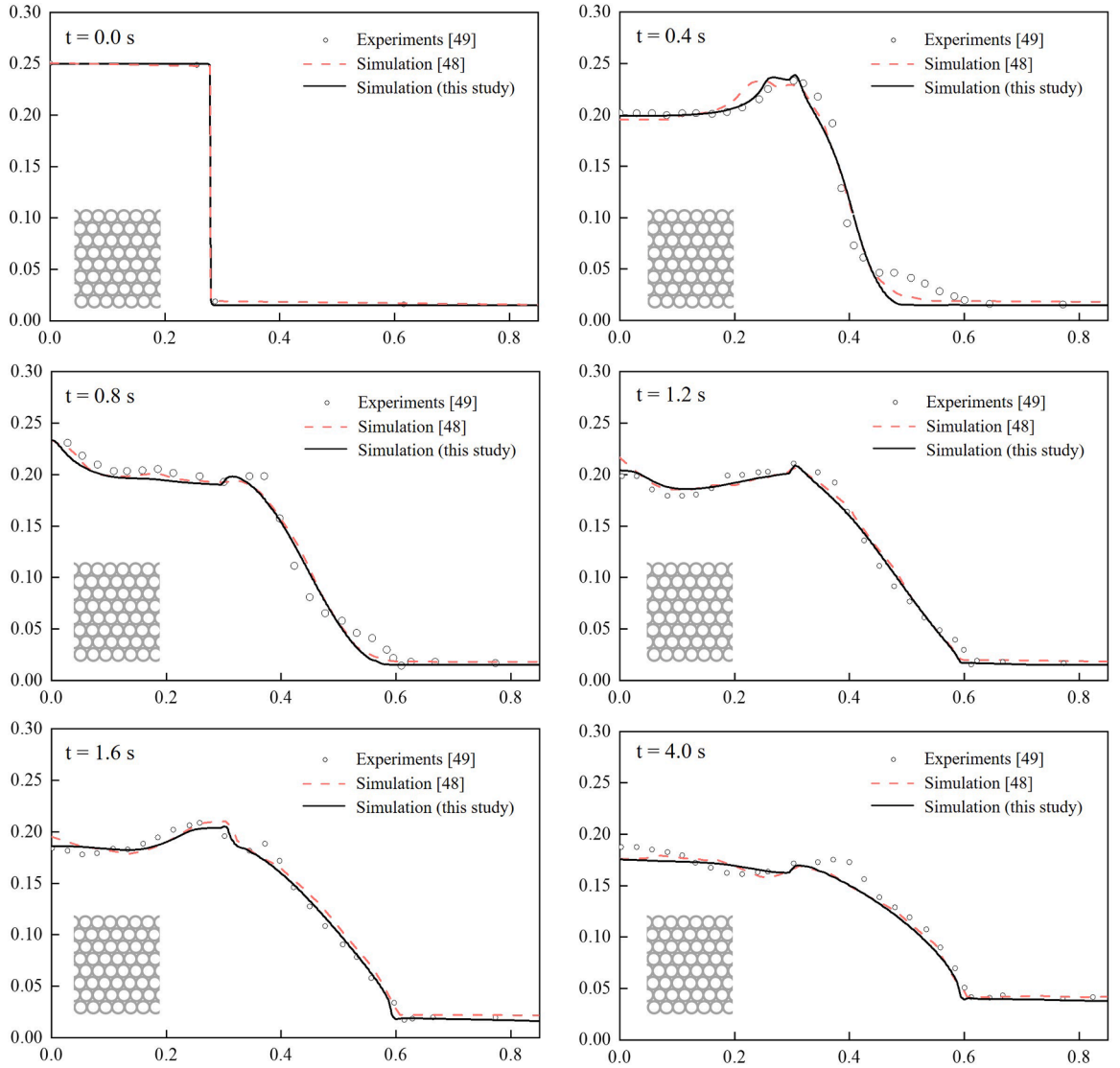

Fig. 18. Comparison among experimental testing data [67], CFD-DEM simulation [66], and the present simulation with $m = 1.0$ and $k_0 = 5 \times 10^{-9}$ m^2 for flow through the glass-beads dam.

coastal protection applications.

3.2.4. Benchmark VI: three-dimensional moving porous structure and pure fluid regions

Benchmark VI examines the three-dimensional coupled interaction of a moored porous structure with two-phase wave-driven flow. The computational setup (Fig. 23A) includes a wave-generating piston, four mooring chains, the porous floating body, and a downstream wave-damping zone. Fig. 23B illustrates the motion of the porous structure and the corresponding configuration changes of the mooring system over one wave period. Note that the chains are shown schematically as straight lines, a simplification that does not affect the computed structural forces.

In contrast to Benchmark V, the moored porous floating structure here undergoes significant forward translation and lateral oscillation due to constraint by the mooring system. Fig. 24A compares the numerical and experimental time histories for rotation angle and x-displacement over one period. The numerical model captures the overall motion trends well, with maximum deviations of approximately 5 % in rotation and 8 % in displacement, both within acceptable margins. Closer inspection reveals the smoother numerical profile lacks the inflection points seen in the experimental displacement curve. This discrepancy aligns with the explanation from Benchmark V: the porous medium is modeled as a continuous equivalent, which introduces possible deviations from the discrete physical experiment. Additional minor discrepancies may stem from uncertainties in measuring centimeter-scale experimental motions.

A grid-convergence study with three resolution levels of successive refinement ratios of 1.6 (10 mm, 16 mm, and 25.6 mm,

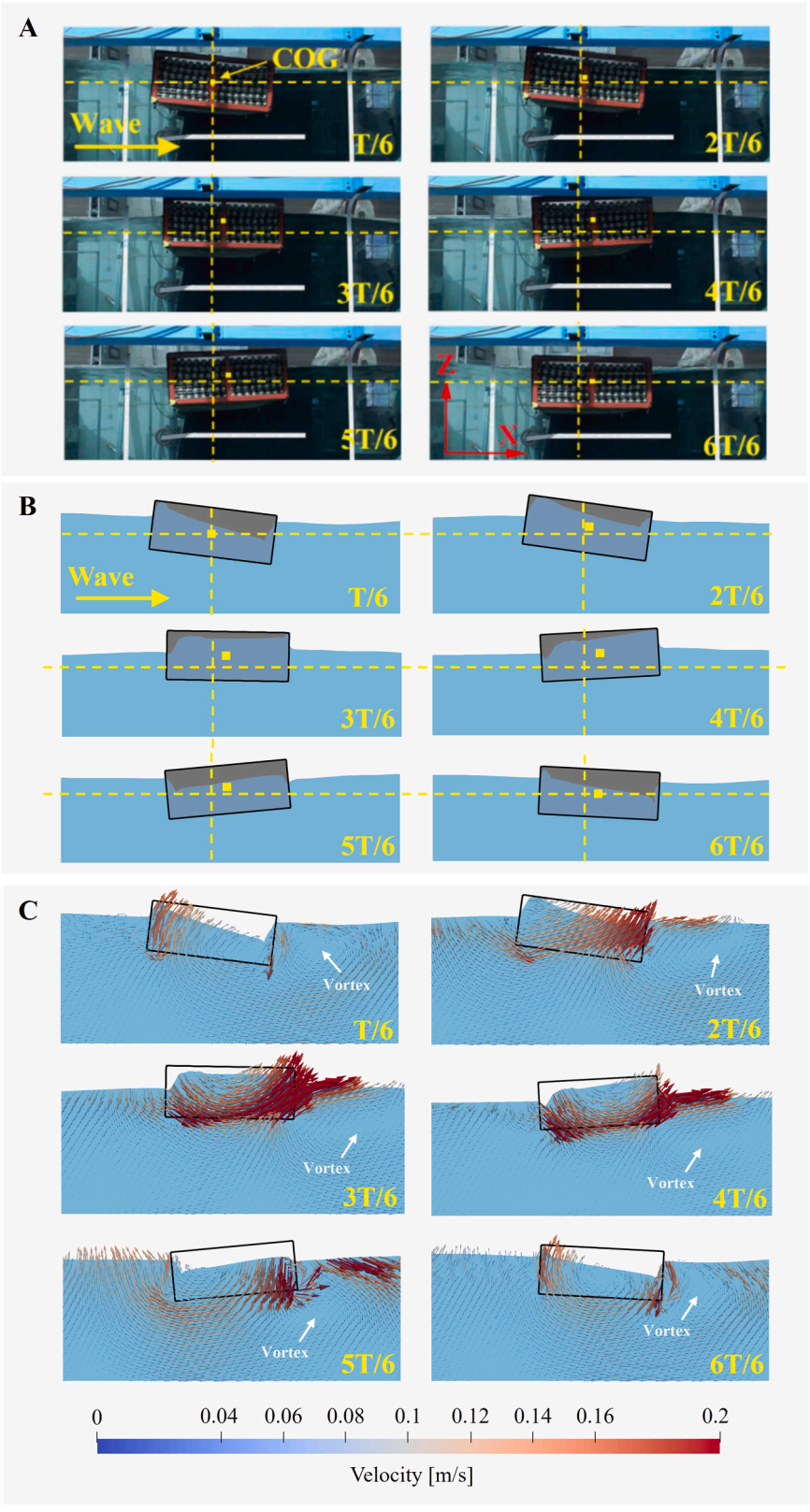

(caption on next page)

Fig. 19. Time-resolved experimental snapshots capturing the dynamic response of the floating porous structure over six characteristic wave phases. (A) Experimental observations [33]; (B) Corresponding simulation results using the proposed method; (C) Velocity vector field predicted by the simulation.

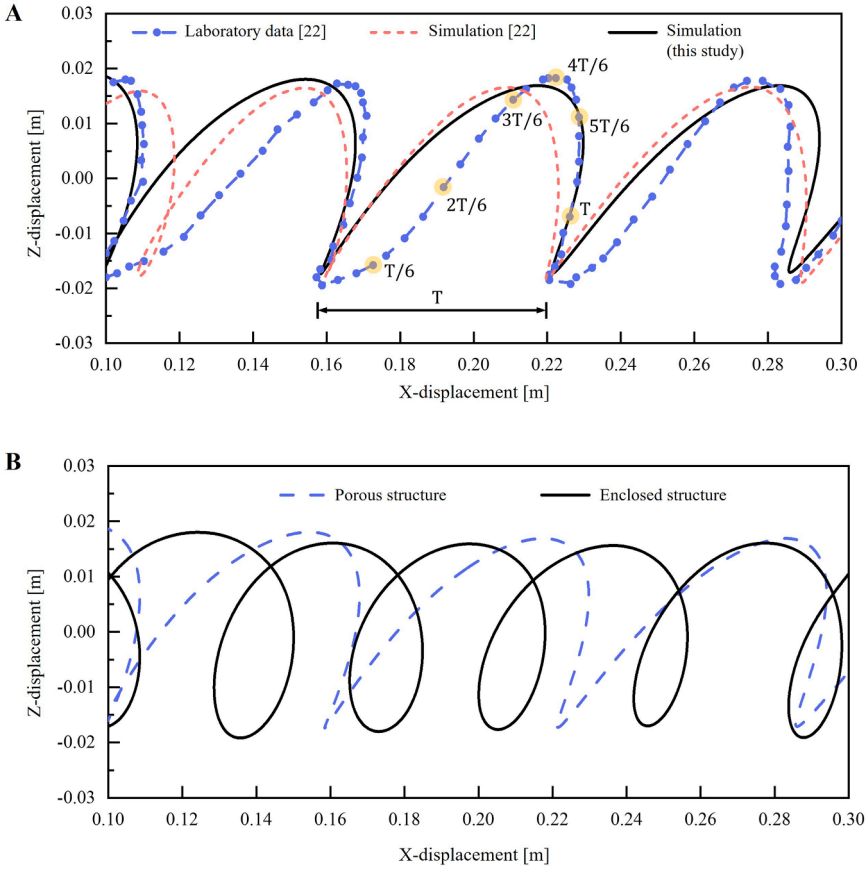

Fig. 20. Comparison of the trajectory of the center of gravity (CoG) of (A) the floating porous structure, including experimental data [33], previous simulation results [33], and results obtained in this study; (B) the floating porous structure and the enclosed structure.

corresponding to 22, 13.7, and 8.6 elements per the smallest vertical structural scale, respectively) further confirms spatial independence. As shown in Fig. 24B, the results from the 10 mm and 16 mm grids are closely aligned (deviations < 3.8 %), while the coarsest mesh (25.6 mm) exhibits significantly larger errors (up to 11 % in rotation and 9.5 % in displacement). This confirms that the 16 mm baseline grid provides a converged solution.

4. Simulation of wave impact on coastal structures

4.1. Model setup

Fig. 25 illustrates the model setup for the illustrative case study on wave impact against coastal structures. The computational domain measures 45 m $\times$ 40 m $\times$ 8 m, discretized with a uniform grid size of 0.015 m, resulting in approximately 4.3 million cells. The time steps for the CFD and DEM simulations are 0.005 s and 0.0005 s, respectively. The solid domain comprises a seawall and 118 cubic armor units, each with a side length of 1.2 m. The armor units have a density of 2500 kg/m^3 and a porosity of 0.25, while the seawall is modeled as an impermeable rigid body. A normal contact stiffness of 529 kN/m and a friction coefficient of 0.6 are assigned to all relevant interfaces. Each block spans approximately 8 grid cells in one direction, satisfying the resolution requirements for resolved CFD-DEM simulations [72]. Executed on an NVIDIA RTX 4070 Ti Super GPU, the simulation of this case for 60 s of physical time was completed within 5.2 h of wall-clock time, showcasing the computational efficiency of the proposed CFD-DEM framework on modern GPU architectures.

The seawall has a curved geometry with a trapezoidal cross-section: 4.3 m in height, 2 m wide at the top, and 7 m at the base. Its total width is 60 m, but to reduce computational cost, only the central 40 m section is simulated. A piston-type wave maker of 1 m

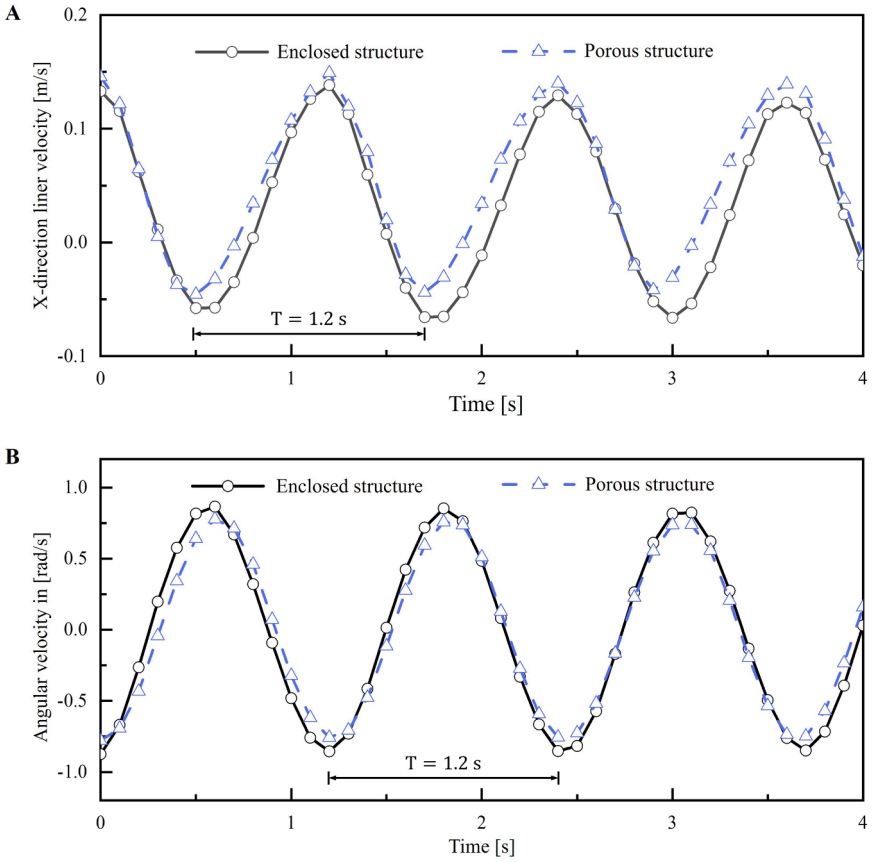

Fig. 21. Comparative profiles of (A) x-direction linear velocity and (B) angular velocity magnitude for porous and enclosed structures under wave loading.

length and 40 m width is placed between x = 3 m and x = 4 m to generate waves, as shown in Fig. 4. A sinusoidal wave with an amplitude of 0.5 m and a period of 4 s is prescribed. Initially, a still water region of height 3.2 m is set in the range x = 0–25 m.

The seawall is modeled as a fixed, impermeable solid. The armor units are modeled either as freely moving porous media or as impermeable solids for comparative analysis. Given that armor units are often constructed from porous concrete with efficient drainage capabilities, the Darcy-Forchheimer model is applied, using the same parameters as in the previous benchmark case. The fluid properties for water and air are consistent with those used in the previous section. This case study serves to verify the capability of the proposed two-phase CFD-DEM framework in modeling complex interactions among waves, free porous blocks, and fixed seawalls.

4.2. *Analysis of simulation results*

Fig. 26 illustrates the fluid distribution and velocity vectors during the initial stage of seawater impact on the armor units and dam structures. First, the top view shown in Fig. 26A clearly indicates that seawater rapidly flows through the gaps between the armor units. Due to the narrowness of these gaps, the flow velocity within them is significantly higher, approximately 1.5 times, compared to the regions not directly obstructed by the armor units (as observed at $t = 0.5$ s). As the wave continues to propagate over the armor units ($t = 1.0$ s to 2.0 s), the velocity within the porous region decreases rapidly, from 0.75 m/s to approximately 0.4 m/s. This reduction is attributed to the additional resistance imposed by the downstream armor units and dam structures as the fluid traverses the porous region.

Following this interaction, a distinct reflected wave is generated due to the combined resistance of the armor units and the dam. Notably, at $t = 2.0$ s, the reflected wave is more pronounced on both lateral sides of the curved dam. This phenomenon arises because the wave initially impacts the central part of the dam before reaching the sides, allowing more time for the wave's potential energy to be converted into kinetic energy, thereby increasing the impact velocity. This increased initial impact velocity on the sides also results in the greater wave height upon passing through the armor-unit gaps, where the wave crests have already reached the top of the dam. This effect is clearly observed in Fig. 26B at $t = 1.0$ s, where the impact velocity of the lateral waves is approximately twice that of the central region. By $t = 4.0$ s, the reflected wave collides and merges with the incoming incident wave, leading to a reduction in wave velocity due to their interaction ($t = 3.0$ s to 4.0 s).

Beyond the initial impact phase, to further investigate the long-term evolution of wave motion, we conducted a simulation

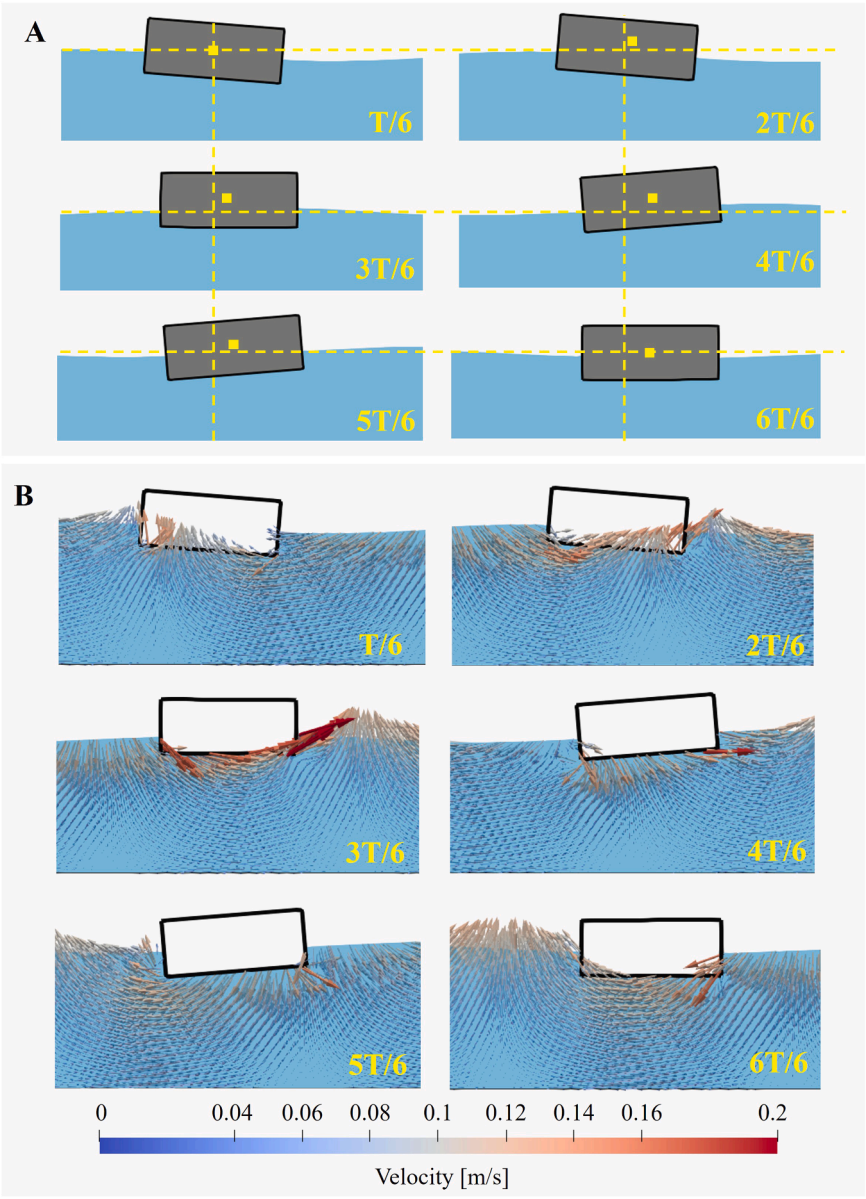

Fig. 22. Time-resolved experimental snapshots capturing the dynamic response of the floating enclosed structure over six characteristic wave phases. (A) Corresponding simulation results using the proposed method; (C) Velocity vector field predicted by the simulation.

spanning one minute and plotted the variation of the total kinetic energy of the water within the computational domain, as shown in Fig. 27. To examine the influence of armor-unit permeability on wave energy dissipation, two different drag force coefficients were considered, represented by the solid and dashed lines in Fig. 27. Specifically, Case I employs a drag force coefficient of 1×10^7 kg/(m^3·s), while Case II uses 1×10^6 kg/(m^3·s), as a reference for the subsequent analysis.

Initially, both cases exhibit identical trends in kinetic energy variation, which is directly related to the prescribed wave-making period in the simulation. At the beginning of the simulation, the prescribed initial fluid field, under the influence of gravity, leads to the conversion of potential energy into kinetic energy, resulting in a large initial impact velocity (see Fig. 26) and correspondingly high initial kinetic energy, as illustrated during 0–4 s in Fig. 27A. However, as described in the previous section, the incident waves interact with the reflected waves, leading to partial cancellation of motion. Combined with the resistance exerted by the armor units and dam structures, this interaction causes a periodic decay in the total kinetic energy. In this early stage, energy dissipation is primarily dominated by internal fluid interactions, and thus the differences between the two drag force coefficients are minimal.

After 30 s, the wave field reaches a quasi-steady state governed primarily by the wave-making conditions. In this regime, the resistance from the armor units and dam becomes the dominant factor driving energy dissipation. Fig. 27B shows an enlarged view of the kinetic energy evolution from 30 s to 60 s, where it is evident that the case with the smaller drag force coefficient consistently

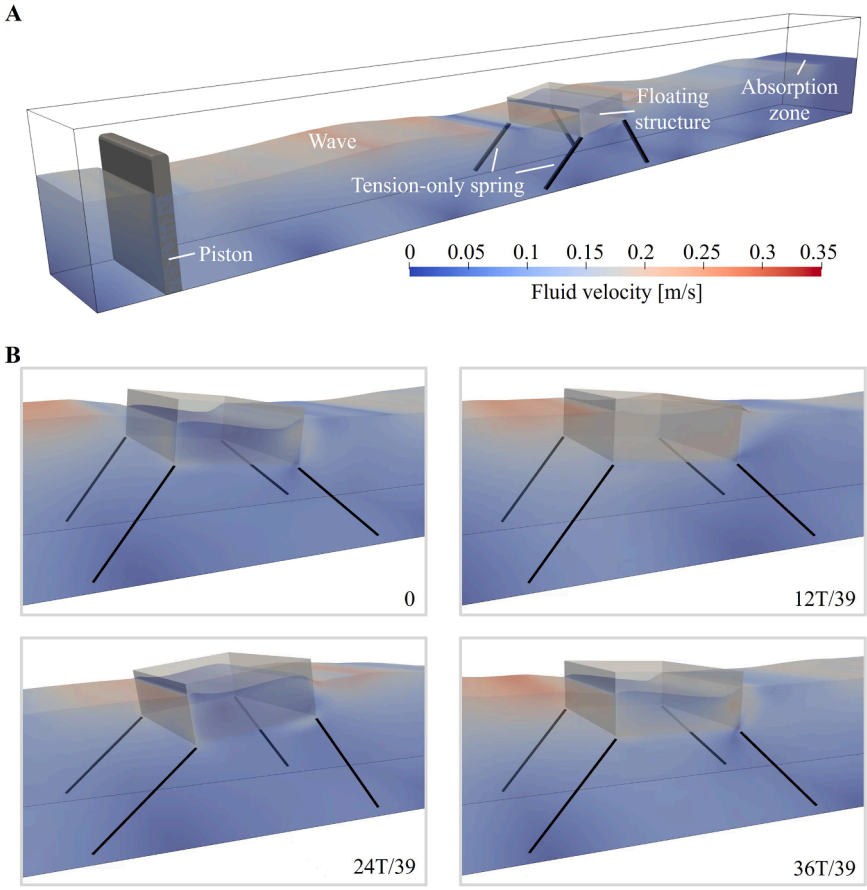

Fig. 23. (A) Schematic illustration of the Benchmark VI model and (B) the corresponding wave-structure motion response at four instants within one wave period ($T = 1.3$ s).

exhibits lower kinetic energy compared to the larger coefficient, with a maximum reduction of up to approximately 8 %. It is important to note that a smaller drag force coefficient corresponds to higher armor-unit permeability, allowing more wave energy to penetrate the armor units and experience additional dissipation due to internal resistance. These findings are consistent with the conclusions drawn in Benchmark V.

To further examine the wave energy dissipation process, Fig. 27C presents the time history of the total kinetic energy of the armor units. This energy is governed by two primary components: the wave kinetic energy and the energy dissipation from friction. The dominant energy transfer pathway involves the wave kinetic energy being converted into the kinetic energy of the armor units via fluid-particle drag force, followed by dissipated through friction. A comparison between the high-permeability (Case II) and low-permeability (Case I) cases reveals key differences. During the period of 2–36 s, the mean kinetic energy for Case II is 200.4 J, 7.3 % higher than that of Case I (2729.8 J). In contrast, from 36–60 s, the mean kinetic energy of Case II is 56.2 J lower. This shift occurs because the low-permeability case exhibits higher wave kinetic energy in the later stage (36–60 s), leading to higher armor unit velocities (Fig. 27B). However, in the earlier stage (2–36 s), the difference in wave kinetic energy is negligible, while the armor units in the high-permeability case possess significantly more kinetic energy. This indicates that a greater portion of wave energy is converted into the kinetic and subsequently dissipated in the porous structures, demonstrating their advantage in promoting wave energy dissipation.

To further investigate the underlying causes of the energy differences observed between the two cases, we focus on the time point at which this discrepancy is most pronounced, namely $t = 36.5$ s, and examine the corresponding differences in wave flow field distributions. Fig. 28 (A and B) presents the velocity field distributions within the wave region for both cases, using the same contour scale with a maximum velocity of 3 m/s. As the wave field has reached a quasi-steady state at this time, the peak velocities are approximately half of those observed during the initial impact phase (Fig. 26). In this context, two key differences are noted: in Case I, due to the lower permeability of the armor units, the wave is able to propagate farther inland, as shown in the magnified insets of Fig. 28 (A and B); moreover, the reflected wave in Case I exhibits a higher velocity compared to Case II, with maximum values of 2.41 m/s and 2.26 m/s, respectively, an increase of approximately 6 %.

To provide further insight, we examine the cross-section I-I ($y = 42$ m) that passes through the region of maximum reflected wave velocity, as indicated in Fig. 28 (A and B). Fig. 28 (C and D) shows the velocity vector fields, flow distributions, and armor-unit

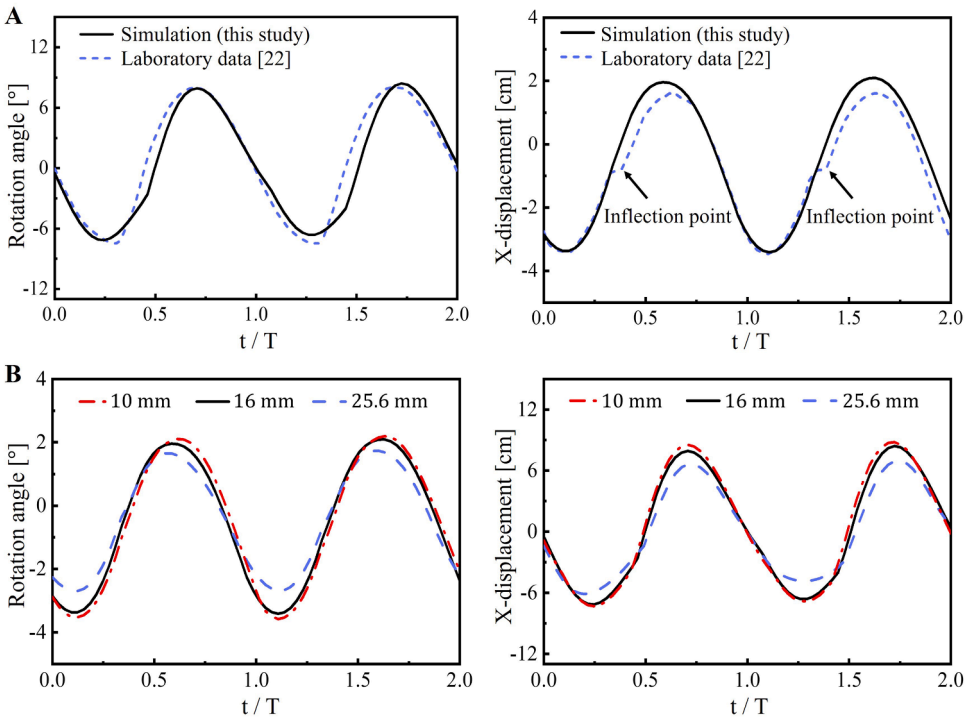

Fig. 24. Validation and convergence study of the floating body motion: (A) Temporal evolution of rotation angle and x-coordinate validated against experimental data [68]; (B) Assessment of grid convergence for the same parameters using mesh sizes of 10 mm, 16 mm, and 25.6 mm.

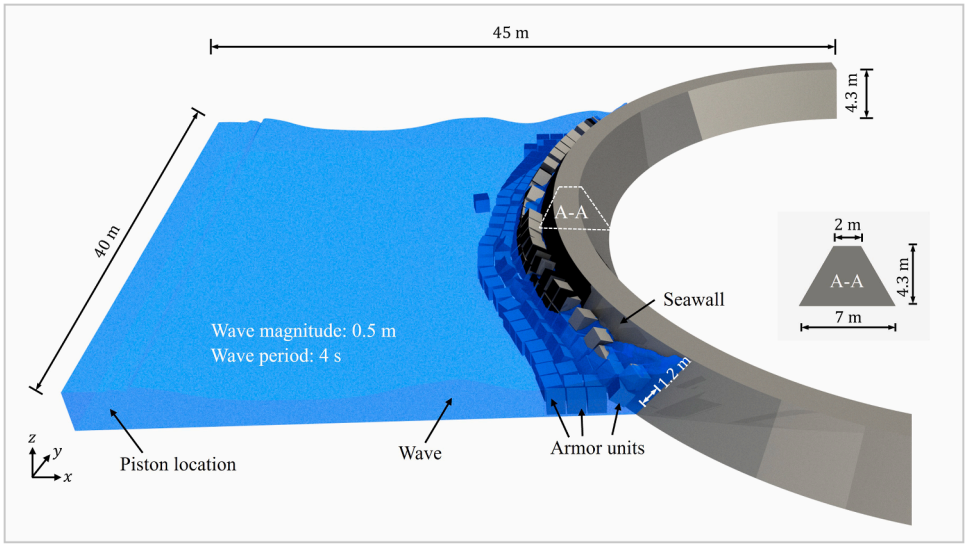

Fig. 25. Schematic diagram of the illustrative case study on wave impact against coastal structures. Waves are generated by a piston-type wave maker, as depicted in Fig. 4.

configurations along this cross-section for both cases. It is evident that in Case I, the lower permeability of the armor units results in the presence of entrapped air, whereas in Case II, the armor units are fully saturated with water. The influence of entrapped air manifests in three key ways: (a) increasing buoyant force on the armor units, which reduces energy dissipation via friction (Fig. 27C); (b) impeding internal water flow, thereby decreasing the volume available for energy dissipation (Fig. 28C); and (c) enhancing water circulation between the armor units and the dam, leading to higher reflected wave heights (Fig. 28E).

Additionally, the reflected wave velocity remains slightly higher in Case I than in Case II, further underscoring the influence of armor-unit permeability on wave energy dynamics. Fig. 28E presents the temporal evolution of the wave height at $x = 20$ m. At this

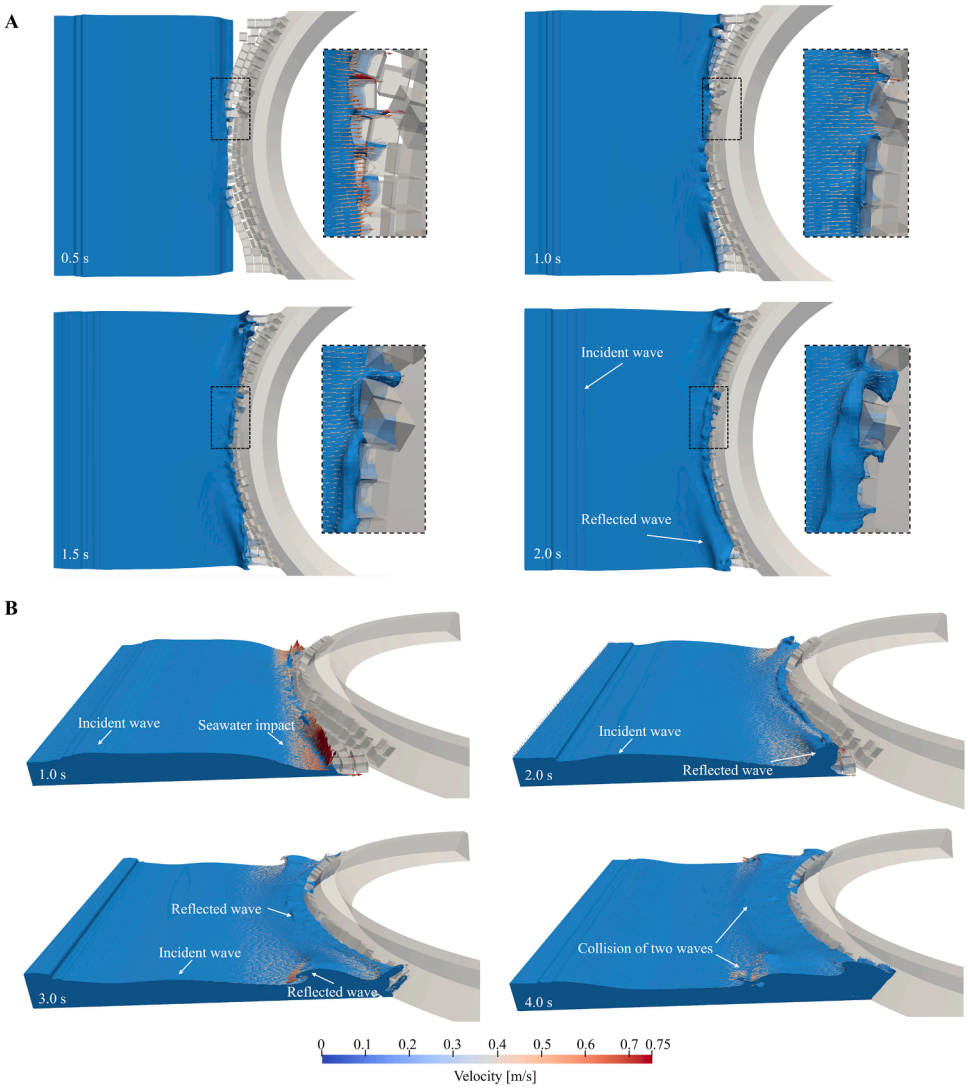

Fig. 26. Simulation results of wave and velocity vectors at different time steps: (A) Top view; (B) Side view.

location, the wave height is governed by both incident and reflected waves. The amplitude of these fluctuations is consistently smaller in the high-permeability case. Over the 10 wave periods shown in Fig. 28E, the mean fluctuation amplitude for the high-permeability case is 0.03 m (or 6 % of the incident wave amplitude) lower than that in the low-permeability case. This finding demonstrates that the high-permeability structure more effectively dissipates wave energy, thereby reducing the overall wave amplitude.

5. Conclusions and outlooks

This study has presented a novel, fully resolved CFD-DEM framework for high-fidelity simulation of multiphase flow interactions with both stationary and mobile porous media of arbitrary geometry. The key contributions of this work are threefold:

(1) A unified micro-continuum formulation: We developed a generalized multiphase flow model that seamlessly integrates pure fluid regions with two distinct types of porous media (coarse-grained Type A and fine-grained, capillary-dominated Type B) within a single set of governing equations. This formulation explicitly resolves the porosity field, eliminating the need for empirical momentum source terms and enabling direct computation of particle-scale hydrodynamic forces.
(2) A robust geometry-aware DEM coupling: The framework incorporates a high-fidelity DEM for arbitrary-shaped particles using an STL-based representation, a barrier-based Incremental Potential Contact (IPC) model to prevent penetration, and a signed distance field (SDF) method for efficient and accurate solid fraction mapping. This allows for the simulation of complex porous structures, their collisions, and their dynamic fluid-structure interactions without geometrical simplification.

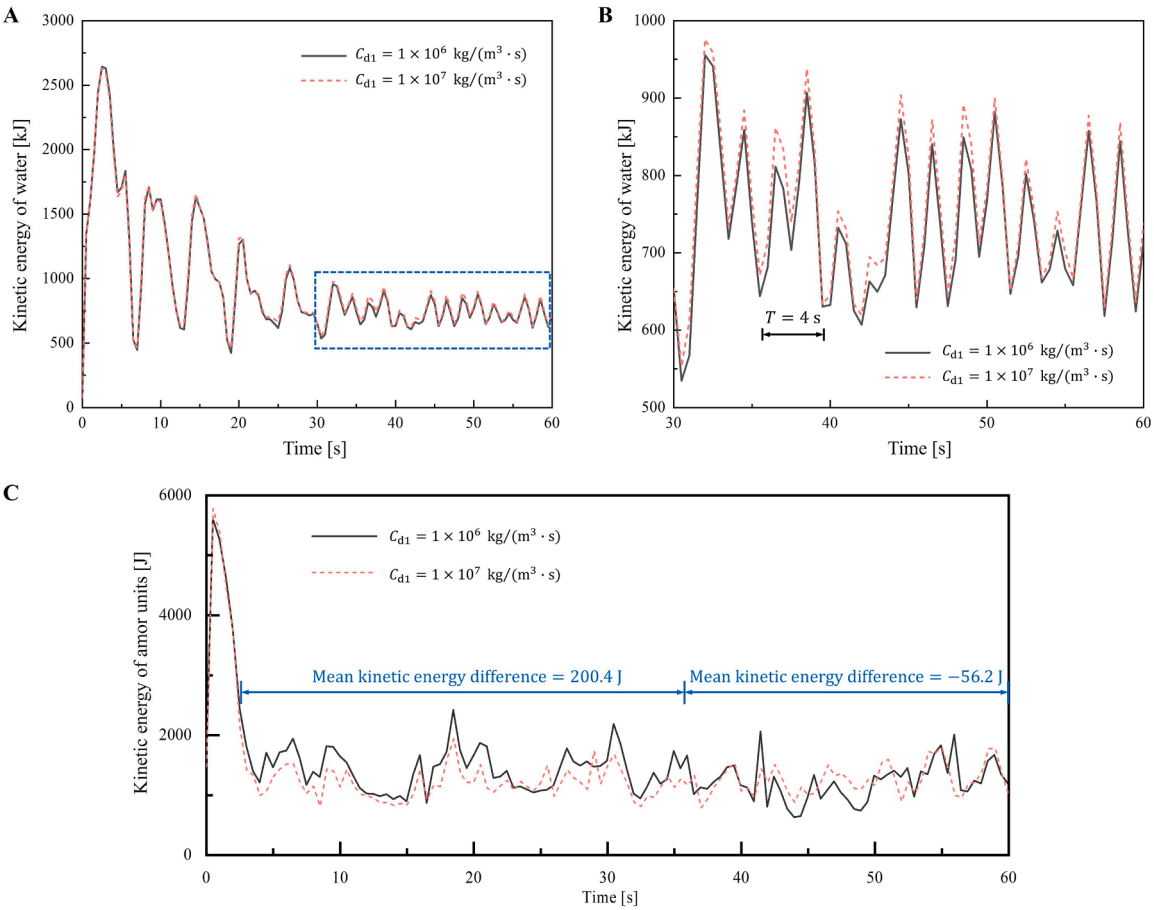

Fig. 27. Evolution of total kinetic energy of water (A-B) and armor units (C) for two different drag coefficients. (A) Full curve (0–60 s); (B) Enlarged view of the 30–60 s interval from (A).

(3) Comprehensive validation and demonstration: We rigorously validated the accuracy and robustness of the framework against six benchmark cases and quantitatively demonstrated its capability to capture critical phenomena including capillarity-gravity equilibrium, viscous fingering, Taylor film formation, transient dam-break seepage, and the six-degree-of-freedom motion of floating porous bodies. The subsequent large-scale application to a coastal defense system with over 100 mobile armor units and a curved seawall confirmed the framework's engineering utility in predicting complex wave dynamics, energy dissipation, and the role of entrapped air.

The results consistently demonstrate that explicitly resolving the geometry and dynamics of porous media is crucial for accurately predicting the complex behavior of coastal fluid-structure systems. The simulations quantitatively show that permeable structures enhance wave energy dissipation not just through drag but also by facilitating fluid flow through interstitial spaces, leading to vortex generation and momentum transfer that are absent in impermeable counterparts.

This integrated approach provides a powerful virtual laboratory for investigating multi-physics problems in coastal engineering, geomechanics, and beyond. Future work will focus on enhancing computational efficiency through adaptive mesh refinement (AMR) [73] and multi-resolution coupling techniques to enable even larger-scale simulations. In particular, AMR can be combined with the cut-cell method [74,75] to handle complex computational domains featuring curved, sloping, or irregular boundaries that commonly arise in industrial and laboratory configurations [76–78]. The framework also sets the stage for exploring related phenomena such as sediment transport, scour, and the fluidization of granular porous media under extreme hydrodynamic loading.

CRediT authorship contribution statement

Tao Yu: Writing – review & editing, Writing – original draft, Visualization, Validation, Software, Methodology, Formal analysis, Data curation, Conceptualization. **Jidong Zhao:** Writing – review & editing, Supervision, Project administration, Funding acquisition.

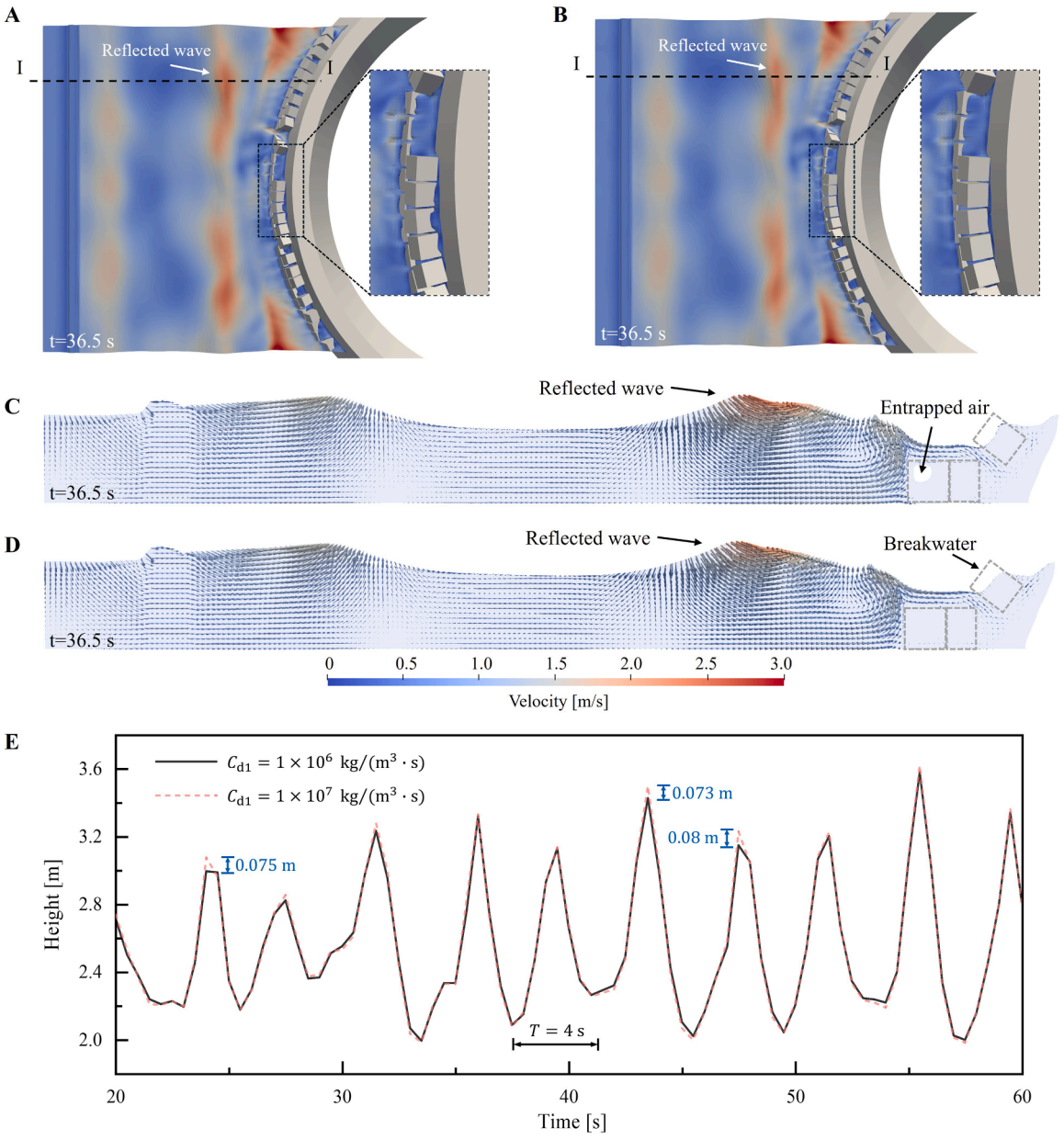

Fig. 28. Water distribution and corresponding velocity field at 36.5 s for drag coefficients of $1 \times 10^7 \mathrm{m}^{-2}$ (A) and $1 \times 10^6 \mathrm{m}^{-2}$ (B). (C) and (D) show the water distribution, velocity vectors, and armor-unit configuration at the $y = 42$ m cross-section at 36.5 s for drag coefficients of $1 \times 10^7 \mathrm{m}^{-2}$ and $1 \times 10^6 \mathrm{m}^{-2}$, respectively. (E) depicts the temporal evolution of the water surface elevation at the intersection of the $x = 20$ m and $y = 42$ m cross-sections.

Declaration of competing interest

The authors declare that they have no known competing financial interests or personal relationships that could have appeared to influence the work reported in this paper.

Acknowledgments

This work was financially supported by State Key Laboratory of Climate Resilience for Coastal Cities (SKLCRCC) (via Project ITC-SKLCRCC26EG01), National Natural Science Foundation of China (Key Project #52439001), and Research Grants Council of Hong Kong (GRF 16203123, 16208224, 16217225, CRF C7085-24G, RIF R6008-24, TRS T22-607/24N, and T22-606/23-R).

Data availability

Data will be made available on request.

References

[1] E.D. Christensen, H.B. Bingham, A.P.S. Friis, A.K. Larsen, K.L. Jensen, An experimental and numerical study of floating breakwaters, Coast. Eng. 137 (2018) 43–58.
[2] J. Dai, C.M. Wang, T. Utsunomiya, W. Duan, Review of recent research and developments on floating breakwaters, Ocean Eng. 158 (2018) 132–151.
[3] N.C. Kraus, The effects of seawalls on the beach: an extended literature review, J. Coast. Res. (1988) 1–28.
[4] N. Hosseinzadeh, M. Ghiasian, E. Andiroglu, J. Lamere, L. Rhode-Barbarigos, J. Sobczak, K.S. Sealey, P. Suraneni, Concrete seawalls: a review of load considerations, ecological performance, durability, and recent innovations, Ecol. Eng. 178 (2022) 106573.
[5] B. Zanuttigh, A. Lamberti, Experimental analysis and numerical simulations of waves and current flows around low-crested rubble-mound structures, J. Waterw. Port Coast. Ocean Eng. 132 (2006) 10–27.
[6] J.A. Zyserman, H.K. Johnson, B. Zanuttigh, L. Martinelli, Analysis of far-field erosion induced by low-crested rubble-mound structures, Coast. Eng. 52 (2005) 977–994.
[7] Z.A. Mokhtar, T.A. Mohammed, B. Yusuf, T.L. Lau, Experimental investigation of tsunami bore impact pressure on a perforated seawall, Appl. Ocean Res. 84 (2019) 291–301.
[8] B. Indraratna, J. Israr, C. Rujikiatkamjorn, Geometrical method for evaluating the internal instability of granular filters based on constriction size distribution, J. Geotech. Geoenviron. Eng. 141 (2015) 04015045.
[9] E. Tutumluer, Y. Qian, Y.M. Hashash, J. Ghaboussi, D.D. Davis, Discrete element modelling of ballasted track deformation behaviour, Int. J. Rail Transp. 1 (2013) 57–73.
[10] E. Koutandos, P. Prinos, X. Gironella, Floating breakwaters under regular and irregular wave forcing: reflection and transmission characteristics, J. Hydraul. Res. 43 (2005) 174–188.
[11] J. Van Der Meer, R. Farajzadeh, W. Rossen, J.D. Jansen, Influence of foam on the stability characteristics of immiscible flow in porous media, Phys. Fluids 30 (2018).
[12] A.T. Chwang, A. Chan, Interaction between porous media and wave motion, Annu. Rev. Fluid Mech. 30 (1998) 53–84.
[13] M. Han, C. Wang, Potential flow theory-based analytical and numerical modelling of porous and perforated breakwaters: a review, Ocean Eng. 249 (2022) 110897.
[14] H. Darcy, fontaines publiques Dijon, 1856.
[15] F. Ph, Wasserbewegung durch boden, Z. Ver. Dtsch. Ing. 45 (1901) 1781–1788.
[16] P.Y. Polubarinova-Kochina, Theory of Ground Water Movement, Princeton university press, 2015.
[17] I.J. Losada, J.L. Lara, R. Guanche, J.M. Gonzalez-Ondina, Numerical analysis of wave overtopping of rubble mound breakwaters, Coast. Eng. 55 (2008) 47–62.
[18] P. Higuera, J.L. Lara, I.J. Losada, Three-dimensional interaction of waves and porous coastal structures using OpenFOAM®. Part I: formulation and validation, Coast. Eng. 83 (2014) 243–258.
[19] H. Wang, Z. Sun, Experimental study of a porous floating breakwater, Ocean Eng. 37 (2010) 520–527.
[20] H. Zhang, B. Sun, Z. Li, F. Wang, Wave attenuation and motion response of floating breakwater with sponge material, Ocean Eng. 277 (2023) 114325.
[21] J. Bear, Dynamics of Fluids in Porous Media, Courier Corporation, 2013.
[22] M. Van Gent, Porous flow through rubble-mound material, J. Waterw. Port Coast. Ocean Eng. 121 (1995) 176–181.
[23] P.L.-F. Liu, P. Lin, K.-A. Chang, T. Sakakiyama, Numerical modeling of wave interaction with porous structures, J. Waterw. Port Coast. Ocean Eng. 125 (1999) 322–330.
[24] D.A. Nield, A. Bejan, Convection in Porous Media, Springer, 2006.
[25] F. Garoosi, A. Kantzas, M. Irani, Numerical simulation of wave interaction with porous structure using the coupled Volume-of-fluid (VOF) and Darcy-Brinkman-Forchheimer model, Eng. Anal. Bound Elem. 166 (2024) 105866.
[26] P. Meakin, A.M. Tartakovsky, Modeling and simulation of pore-scale multiphase fluid flow and reactive transport in fractured and porous media, Rev. Geophys. 47 (2009).
[27] G. Zhang, D. Tang, H. Wen, J. Chen, A modified weakly compressible smoothed particle hydrodynamics mixture model for accurate simulation of wave and porous structure interaction, Phys. Fluids 36 (2024).
[28] M. Osorno, M. Schirwon, N. Kijanski, R. Sivanesapillai, H. Steeb, D. Göddeke, A cross-platform, high-performance SPH toolkit for image-based flow simulations on the pore scale of porous media, Comput. Phys. Commun. 267 (2021) 108059.
[29] M. Chaaban, Y. Heider, B. Markert, A multiscale LBM–TPM–PFM approach for modeling of multiphase fluid flow in fractured porous media, Int. J. Numer. Anal. Methods Geomech. 46 (2022) 2698–2724.
[30] H. Xu, B. Guo, G. Yu, Y. Zhou, F. Wang, Multi-physics modeling of thermochemical storage in porous medium reactors using the lattice Boltzmann method for heat storage applications: bridging pore-scale dynamics and macroscopic performance, J. Energy Storage 114 (2025) 115761.
[31] A.M. Aly, C. Huang, W. Alhejaili, S.-W. Lee, Fractional dynamics and nonlinear mixing in multi-phase porous flow: a hybrid SPH–machine learning framework, Chaos Solit. Fract. 199 (2025) 116841.
[32] W. Wu, Y. Yang, H. Zheng, L. Zhang, N. Zhang, Numerical manifold computational homogenization for hydro-dynamic analysis of discontinuous heterogeneous porous media, Comput. Methods Appl. Mech. Eng. 388 (2022) 114254.
[33] Y. Dong, W. Tan, H. Chen, J. Yuan, Numerical modeling of wave interaction with a porous floating structure consisting of uniform spheres, Phys. Fluids 36 (2024).
[34] Z. Lai, J. Zhao, S. Zhao, L. Huang, Signed distance field enhanced fully resolved CFD-DEM for simulation of granular flows involving multiphase fluids and irregularly shaped particles, Comput. Methods Appl. Mech. Eng. 414 (2023) 116195.
[35] M. Luo, X. Su, E. Kazemi, X. Jin, A. Khayyer, Review of smoothed particle hydrodynamics modeling of fluid flows in porous media with a focus on hydraulic, coastal, and ocean engineering applications, Phys. Fluids 37 (2025).
[36] K. Shwetank, D. Deb, R. Pramanik, Coupled meshfree (SPH) and grid based (FDM) procedures for modeling fluid flow through deformable porous media, Int. J. Rock Mech. Min. Sci. 170 (2023) 105494.
[37] W.-H. Yuan, J.-X. Zhu, K. Liu, W. Zhang, B.-B. Dai, Y. Wang, Dynamic analysis of large deformation problems in saturated porous media by smoothed particle finite element method, Comput. Methods Appl. Mech. Eng. 392 (2022) 114724.
[38] H. Li, Y. Zhao, J. Li, H. Yin, C. Song, M. Hao, CFD-DEM investigation on continuous invasion behaviors of particles and evolution of pore clogging in porous media, Comput. Geotech. 189 (2026) 107675.
[39] Z. Wang, Y. Teng, M. Liu, A semi-resolved CFD–DEM approach for particulate flows with kernel based approximation and hilbert curve based searching strategy, J. Comput. Phys. 384 (2019) 151–169.
[40] F.J. Carrillo, I.C. Bourg, C. Soulaine, Multiphase flow modeling in multiscale porous media: an open-source micro-continuum approach, J. Comput. Phys.: X 8 (2020) 100073.
[41] J. Roenby, B.E. Larsen, H. Bredmose, H. Jasak, A new volume-of-fluid method in OpenFOAM, Marine vi: proceedings of the vi international conference on computational methods in marine engineering, CIMNE (2017) 266–277.
[42] H. Rusche, Computational Fluid Dynamics of Dispersed Two-Phase Flow at High Phase fractions, Ph. D. Thesis, University of London, 2002.
[43] M.T. Van Genuchten, A closed-form equation for predicting the hydraulic conductivity of unsaturated soils, Soil Sci. Soc. Am. J. 44 (1980) 892–898.

[44] R.H. Brooks, Hydraulic Properties of Porous Media, Colorado State University, 1965.
[45] Z. Wang, W. Yan, W.K. Liu, M. Liu, Powder-scale multi-physics modeling of multi-layer multi-track selective laser melting with sharp interface capturing method, Comput. Mech. 63 (2019) 649–661.
[46] P. Forchheimer, Ver Wasserbewegung, Dtsch. Ing. 45 (1901) 1782–1788.
[47] G. Dagan, Flow and Transport in Porous Formations, Springer Science & Business Media, 2012.
[48] A. Di Renzo, F.P. Di Maio, Comparison of contact-force models for the simulation of collisions in DEM-based granular flow codes, Chem. Eng. Sci. 59 (2004) 525–541.
[49] A.B. Stevens, C. Hrenya, Comparison of soft-sphere models to measurements of collision properties during normal impacts, Powder Technol. 154 (2005) 99–109.
[50] H. Zhu, Z. Zhou, R. Yang, A. Yu, Discrete particle simulation of particulate systems: theoretical developments, Chem. Eng. Sci. 62 (2007) 3378–3396.
[51] R. Bhaskaran, L. Collins, Introduction to CFD Basics, Cornell University-Sibley School of Mechanical and Aerospace Engineering, 2002, pp. 1–21.
[52] T. Yu, J. Zhao, Semi-coupled resolved CFD–DEM simulation of powder-based selective laser melting for additive manufacturing, Comput Methods Appl. Mech. Eng. 377 (2021) 113707.
[53] N. Das, Modeling Three-Dimensional Shape of Sand Grains Using Discrete Element Method, University of South Florida, 2007.
[54] Z. Shen, G. Wang, D. Huang, F. Jin, A resolved CFD-DEM coupling model for modeling two-phase fluids interaction with irregularly shaped particles, J. Comput. Phys. 448 (2022) 110695.
[55] B. Zhou, J. Wang, Generation of a realistic 3D sand assembly using X-ray micro-computed tomography and spherical harmonic-based principal component analysis, Int. J. Numer. Anal. Methods Geomech. 41 (2017) 93–109.
[56] S. Galindo-Torres, A coupled discrete element lattice Boltzmann method for the simulation of fluid–solid interaction with particles of general shapes, Comput. Methods Appl. Mech. Eng. 265 (2013) 107–119.
[57] M. Wang, Y. Feng, T. Qu, T. Zhao, A coupled polygonal DEM-LBM technique based on an immersed boundary method and energy-conserving contact algorithm, Powder Technol. 381 (2021) 101–109.
[58] C.M. Pereira, A.L. Ramalho, J.A. Ambrósio, A critical overview of internal and external cylinder contact force models, Nonlinear Dyn. 63 (2011) 681–697.
[59] H.A. Navarro, M.P. de Souza Braun, Determination of the normal spring stiffness coefficient in the linear spring–dashpot contact model of discrete element method, Powder Technol. 246 (2013) 707–722.
[60] M. Li, Z. Ferguson, T. Schneider, T.R. Langlois, D. Zorin, D. Panozzo, C. Jiang, D.M. Kaufman, Incremental potential contact: intersection-and inversion-free, large-deformation dynamics, ACM Trans. Graph. 39 (2020) 49.
[61] Y. Zhao, J. Choo, Y. Jiang, M. Li, C. Jiang, K. Soga, A barrier method for frictional contact on embedded interfaces, Comput. Methods Appl. Mech. Eng. 393 (2022) 114820.
[62] A.A. Shirgaonkar, M.A. MacIver, N.A. Patankar, A new mathematical formulation and fast algorithm for fully resolved simulation of self-propulsion, J. Comput. Phys. 228 (2009) 2366–2390.
[63] R.I. Issa, Solution of the implicitly discretised fluid flow equations by operator-splitting, J. Comput. Phys. 62 (1986) 40–65.
[64] P. Horgue, M. Prat, M. Quintard, A penalization technique applied to the “volume-of-fluid” method: wettability condition on immersed boundaries, Comput. Fluids 100 (2014) 255–266.
[65] P. Aussillous, D. Quéré, Quick deposition of a fluid on the wall of a tube, Phys. fluids 12 (2000) 2367–2371.
[66] E. Jafari, M.M. Namin, P. Badiei, Numerical simulation of wave interaction with porous structures, Appl. Ocean Res. 108 (2021) 102522.
[67] P. Lin, Numerical Modeling of Breaking Waves, Cornell University, 1998.
[68] K. Luo, Y. Dong, J. Yuan, Impact of mooring configurations on wave attenuation of porous floating breakwater: a comparative experimental study, Coast. Eng. (2025) 104823.
[69] P. Horgue, C. Soulaine, J. Franc, R. Guibert, G. Debenest, An open-source toolbox for multiphase flow in porous media, Comput. Phys. Commun. 187 (2015) 217–226.
[70] M. Graveleau, C. Soulaine, H.A. Tchelepi, Pore-scale simulation of interphase multicomponent mass transfer for subsurface flow, Transp. Porous Media 120 (2017) 287–308.
[71] J. Maes, C. Soulaine, A unified single-field volume-of-fluid-based formulation for multi-component interfacial transfer with local volume changes, J. Comput. Phys. 402 (2020) 109024.
[72] A. Hager, C. Kloss, S. Pirker, C. Goniva, Parallel resolved open source CFD-DEM: method, validation and application, J. Comput. Multiph. Flows 6 (2014) 13–27.
[73] T. Yu, J. Zhao, GPU-optimized adaptive mesh refinement for scalable two-phase resolved CFD-DEM simulations on unstructured hexahedral grids, Comput. Phys. Commun. (2025) 109939.
[74] Y. Lu, S. Rane, A. Kovacevic, Evaluation of cut cell cartesian method for simulation of a hook and claw type hydrogen pump, Int. J. Hydrog. Energy 47 (2022) 23006–23018.
[75] P.G. Tucker, Z. Pan, A Cartesian cut cell method for incompressible viscous flow, Appl. Math. Model. 24 (2000) 591–606.
[76] A. Hager, C.D.L. für partikuläre Strömungen, D.-I.D.C. Goniva, CFD–DEM on Multiple Scales, an Extensive Investigation of Parti-cle–Fluid Interactions, Johannes Kepler University Linz, Linz, 2014.
[77] J. Mao, L. Zhao, Y. Di, X. Liu, W. Xu, A resolved CFD–DEM approach for the simulation of landslides and impulse waves, Comput. Methods Appl. Mech. Eng. 359 (2020) 112750.
[78] C. Li, Y. Zhang, J. Shen, W. Zhang, Coupled simulation of fluid-particle interaction for large complex granules: a resolved CFD-DEM method for modelling the airflow in a vertical fixed bed of irregular sinter particles, Particuology 90 (2024) 292–306.